UNIVERSITY OF THESSALY

DEPARTMENT OF MECHANICAL ENGINEERING

SIMULATION AND STUDY OF HEAT TREATMENT EFFECTS ON ALUMINIUM ALLOYS

By

Katsantonis Apostolopoulos Ioannis

Supervisor Prof. Gregory N. Haidemenopoulos

Submitted to the Department of Mechanical Engineering in September 2022

in partial fulfillment of requirements for the degree of

Mechanical Engineer

Thesis Committee:

1st member (Supervisor)	Professor G.N. Haidemenopoulos Department of Mechanical Engineering, University of Thessaly
2nd member	Associate Professor E. Bouzakis Department of Mechanical Engineering, University of Thessaly
3rd member	Dr. H. Kamoutsi Department of Mechanical Engineering, University of Thessaly

Abstract

Aluminum alloys are steadily growing in popularity for industrial uses. They combine lightness with great strength, easy processing, and fairly low manufacturing costs. Key part for this success is the heat treatment they undergo in order to achieve the desired mechanical properties. This study is focused on the effects of heat treatments on the microstructure of aluminum alloys 6xxx series and especially on the 6060 Al-alloy. The target is the characterization of extruded and aged specimens provided by Alumil as well as to perform a microstructure analysis through TEM and SEM-EDX methods. Afterwards precipitation calculations through computational thermodynamics are to be performed in order to document the microstructural evolution during aging and propose if possible alternate aging procedures that enhance the mechanical properties of the final product. Additionally, tensile tests are scheduled, in order to confirm the simulation results concerning the yield strength. Finally, an algorithm that, provided experimental measures and tensile test results for calibration purposes, can predict the flow stress based on stress-strain evolution of the material in any condition from as cast to aged.

Table of contents

List of Figures

List of Tables

Acknowledgments

First of all, I would like to thank Professor Gregory N. Haidemenopoulos for all his guidance and help through this project and for giving me the opportunity to be a part of this study.

I would also like to thank Associate Professor Emmanouil Bouzakis and Dr. Helen Kamoutsi for participating in my thesis committee.

I want to express my gratitude to Dr. Ioannis Aristeidakis and Dr. Margianna Tzini for their tireless support, the immeasurable amount of help, guidance, knowledge and patience they showed me.

Finally, I would like to thank my friends and family for the support and motivation they gave me before and throughout this time.

1. Introduction

Aluminum alloys are ever increasing in popularity among the construction and design crews all over the world. The characteristics that command that popularity are their combination of high strength, formability, extreme durability, excellent corrosion resistance and low density. A very widely used category of Al-alloys is the 6xxx series. 6xxx Series alloys are heat-treatable, which means that they acquire their optimum mechanical properties through a process of thermal treatment. These are the Al-Mg-Si alloys (Mg and Si additions of around 1%) and are found widely throughout the welding fabrication, industry, used predominantly in the form of extrusions and incorporated in many structural components. The addition of magnesium and silicon to aluminum enables the formation of a magnesium-silicide intermetallic compound, which can contribute to precipitation strengthening through an aging heat treatment. Secondary alloying elements might include Mn, Cu, Zn, Ti, Zr and Fe in small quantities. Especially Fe and Mn can play an important role on the microstructural and mechanical properties of the material, due to the formation of stable intermetallic compounds with Si and Al, most notably the α-, and β-AlFeSi phases. The 6060 alloy is commonly used in extrusion applications and is categorized as medium strength heat treatable alloy containing 0.3 to 0.6% of Silicon and 0.35 to 0.5% of Magnesium. Its solidus temperature is around 600 °C depending on the composition, its ultimate tensile strength ranges from 140-230 MPa and its yield strength from 70-180 MPa. It is known for exceptional corrosion resistance, good formability, weldability and anodizing response. The table of chemical composition according to EN573-3 for 6060 Al-Alloys is provided from [1]:

Table 1: 6060 Al-alloy chemical composition table

Si	Fe	Cu	Mn	Mg	Cr	Zn	Ti	Others	
								Each	total
0.30-0.6	0.10-0.30	max. 0.10	max. 0.10	0.35-0.6	max. 0.05	max. 0.15	max. 0.10	max 0.05	max. 0.15

The mechanical properties of an alloy are influenced by the microstructure, which depends on the thermomechanical treatment that the material has undergone. Thus, in order to achieve specific mechanical properties, it is necessary to control the microstructural evolution via processing.

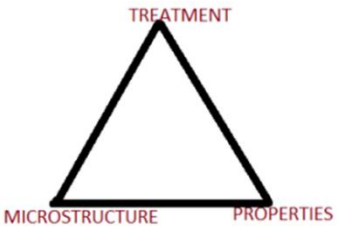

Figure 1: Triangle: Treatment-Microstructure-Properties.

In Figure 2, a sketch of the different process steps, often found in extrudable aluminum alloys, is depicted. First, the alloying elements are added during *melt treatment*. The main strengthening contribution is a result of adding Mg and Si to form Mg_2Si strengthening precipitates. Melt treatment is followed by casting. *Casting* is a technical process in which a molten metal acquires the desired shape (ingots for rolling process or billets for extrusion). 6060 aluminum alloys are normally casted in the foundry in the form of cylindrical columns called billets. The metal solidifies after the casting process. The microstructure of the casting consists of three zones related to the size and morphology of the grains: chill, columnar and equiaxed zone.

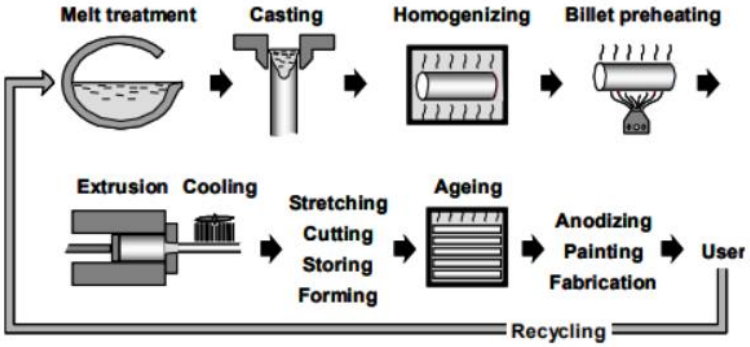

Figure 2: Sketch of the different process steps.

The solidification during casting results in a modification of the composition from point to point, i.e. segregation. Micro-segregation is found when composition changes in the dendritic regions due to the rejection of the second component and is more important at the borders of the columnar zone. It is a significant problem in castings because it affects the mechanical properties, due to the heterogeneity in the distribution of the alloying elements in the grain scale and the formation of undesired Fe-bearing intermetallics, like the β-AlFeSi and π-phase, in the form of coarse particles with sharp edges. This problem is more important when thermal treatments follow the casting to strengthen the alloy. Regarding the 6xxx alloys in particular, segregation results in regions low in Mg and Si causing an inhomogeneous formation of Mg_2Si during the aging process.

The next process is *homogenization*. During homogenization, the alloy is heated below the solidus in order for the alloying elements to uniformly redistribute in the matrix and the various intermetallics to dissolve. In this way, the microstructure of aluminum is changes as elements diffuse from the grain boundaries to the inside of the grain and the β- to α-AlFeSi transformation takes place. Additionally, dispersoid particles comprised of the α-Mn phase, form on the grain boundaries as well as inside the grains. Homogenization is followed by a rapid cooling procedure During which some precipitates can form as the supersaturation of alloying elements in the solid solution increases. The rapid rate of cooling is important for minimizing the formation of coarse particles that can hinder extrusion.

Commonly, 6060 aluminum alloys are extruded after homogenization. The billet is *preheated* (450-500°C) in order to reduce yield strength, dissolve Mg_2Si particles that might have formed during homogenization cooling and permit extrusion to take place. *Extrusion* is a process used to create objects of fixed cross-sectional profile. The microstructure of Aluminum extrusion influences mechanical properties of the alloy and its surface quality. Wherever it is observed more plastic deformation, recrystallization can take place. Non-

recrystallized structure is preferred because although large grains reduce formability, and they inhibit the formation of Precipitation Free Zones (PFZ) during aging. Extrusion is followed by *quenching* to inhibit precipitation and create a super saturated solid solution.

The final stage is aging. *Aging* is the process by which a uniform dispersion of precipitates is created from the supersaturated solid solution. Aging determines the final mechanical properties of the material. Based on all these treatments, certain factors are controlled to obtain an alloy with a specific microstructure and the desired mechanical properties. For the 6060 aluminum alloys, the most common aging treatments are the T3, T5, T6 and T6I6 methods.

The target of this study is to model and describe the aging treatment and present initial results from the simulation of aging for the 6060 Al-alloy. Computational thermodynamic and kinetic modeling is used for the description of microstructural evolution during aging, aiming at the improvement of the final properties of 6060 Al-alloy.

1.1 Materials Processing

The 6060 aluminium alloy is characterized by 3 main internal transformations. During homogenization, the following alterations take place: β-AlFeSi to α-AlFeSi transformation and dissolution of Mg_2Si and re-precipitation during cooling. The non-soluble iron intermetallics are transformed to α-AlFeSi with a more rounded morphology that won't shear or rapture the microstructure of the alloy during extrusion [2]. The second transformation is crucial to strengthening the alloy, as the Mg_2Si particles which are present from solidification as large particles inside the material are dissolving. During homogenization cooling Mg_2Si re-precipitates as a fine dispersion of small, fully or semi coherent particles throughout the body of the alloy and redissolves during the preheating and extrusion processes. Finally, during aging nucleation and growth of the β" phase takes place, which is the principal factor for strengthening of the alloy. Depending on composition and processing, numerus metastable phases of the Mg_2Si family, like the U1, U2, B, β'' and β' phases can precipitate, with varying degrees of coherency with the matrix. At early stages of aging, small and fully coherent metastable particles nucleate and grow, driven by the minimization of the surface energy. At later stages of aging, coherency can be lost as the radius reaches a critical value, or the formation of a different Mg_2Si family particle takes place as it becomes more energetically favorable. At the point where full coherency is lost, usually coinciding with the transition from β'' to β' precipitation, peak hardness is observed as the strengthening mechanism changes from coherency to Orowan strengthening.

After solution annealing, Mg_2Si particles that precipitated during homogenization, are dissoluted into the matrix again as the material reaches supersaturated solid state. Precipitation begins during cooling after homogenization or extrusion. Diffusion is limited during cooling due to the high cooling rates and the growth of precipitates is inhibited, however nucleation of new particles can still take place. It is often observed through 3DAP (3D atom probing), the vacancies in the supersaturated matrix, are covered with meta-stable Mg-Si co-clusters which are comprised of solute atoms with a ratio of Mg:Si close to 1. These are small, fully coherent nuclei of metastable β-family particles that form during the first part of cooling, when the temperatures are higher. Their activation energy for precipitation

is very small due to a low interfacial energy, and although the driving force for their formation is smaller than this of the stable β phase, they form first as it is easier to nucleate. It is observed through 3DAP (3D atom probing) that the firstly shaped clusters are comprised from 2-10 solute atoms and a wide variety of sizes and irregular cluster shapes is observed. During the first stages of aging, they grow and restructure to form different metastable β-family intermetallics, as the bulk Gibbs energy term and the elastic strain energy term associated with the lattice distortion of the matrix around the particles, dominate over the surface energy terms. The interplay among the bulk energy for formation, the interfacial energy and the elastic strain energy gives rise to the metastable precipitation sequence, starting for fully coherent phase particles with relatively high strain energy and gradual loss of coherency to decrease the strain energy and move towards the equilibrium phase of β-Mg_2Si.

1.2 Typical 6060 Al-alloys aging heat treatments

Typical aging heat treatments of 6xxx Al alloys include the *T3, T5*, *T6* and *T6I6* processes.

T3 aging corresponds to natural aging. When natural aging procedure is followed, after quenching, the material remains at RT. This technique does not trigger diffusion, which is a heat driven process. This, results to further coarsening of the co-clusters formed during extrusion cooling. The number of solute atoms contained in the cluster becomes higher, ranging from 30 to 100, and their shape is rounder. TEM (transmission electron microscopy) is now able to resolve these clusters, referred as coherency zones. The main issue with this type of aging is that the co-clusters do not provide the material with a substantial amount of strength, as they are big, coherent particles that are shearable by dislocations, exhibiting relatively low resistance to dislocation movement. The strength that the co-clusters provide, is proportional to the number of the cluster formed, on the contrary of any classic strengthening mechanism, where strength is depended on the square root of their volume fraction. As it occurs, natural aging has very limited practical use in today's industry standards for the 6xxx aluminum alloys, except when very high ductility is required where natural aging is the way to go.

T6 and T6I6 are the two main aging procedures used for 6xxx aluminium alloys. They are essentially the same in their core but with a slight, albeit important difference. The material is treated in both procedures isothermally usually at approximately 180°C (temperature can vary between 160-190°C, depending on composition). During T6I6, after treating at 180°C for a few minutes immediately after quenching, the material is stored for an hour or less at room temperature and then reheated to the aging temperature. The key word in this process is immediately. In the standard T6, the material is continuously baked at 180°C. The difference is that when the material is treated immediately after quenching, the excessive growth of the co-clusters is avoided. This is crucial as these co-clusters have a high solvus temperature. As they are coherent particles, their free energy decreases and they cannot be dissolved at the aging temperature. T6I6 mitigates this issue, because the vacancies that are left in the matrix, are covered by pre-β'' particles, which are nucleation points for β phase. The procedure of β'' nucleation is sped up as there are significantly less co-clusters to be dissolved at aging temperature and the pre-β" particles are ready to become β" phase. Moreover, T6I6 provides with greater control of coarsening at these early stages and helps

to retain the co-clusters size relatively small. This leads to more β'' nucleation points as the bigger co-clusters do not get dissolved during 180°C treatment and subsequently do not turn

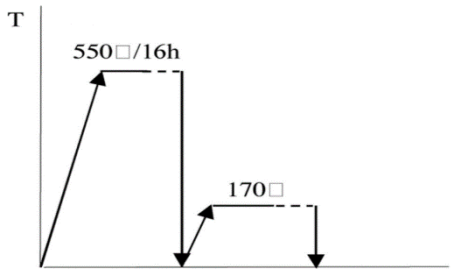

Figure 3: Homogenization and T6 aging procedure

into pre-β'' phase. Also, as the particles do not grow, a finer dispersion is achieved. The RT storage period afterwards, helps with the slight coarsening and stabilization of the existing co-clusters, lowering their total energy.

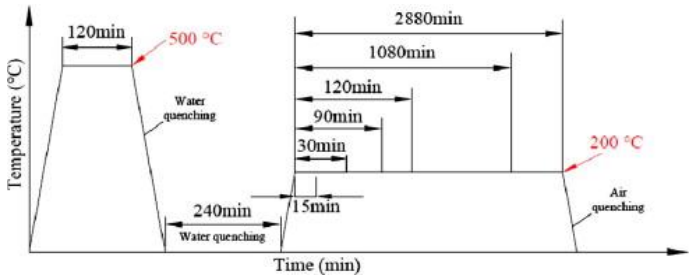

Figure 4: Experimental T6I6 interrupted aging, with different aging times

T5 and double T5 aging is a 2-step aging procedure where the material does not undergo through solution treatment. The alloy is first heated and held to a T1 temperature. Immediately after, it gets heated to a T2 temperature, where T2>T1 where it is again held and then it is cooled to RT. Typical temperatures for aluminum alloys are between 150-200 ^{o}C for T1 and 200-250 ^{o}C for T2, while the maximum time needed in the furnace is determined at 270 minutes as provided by [3]. The main mechanism employed is the precipitation and coarsening of the co-clusters to a critical radius during the hold at T1. Then, with the switch to T2 all the clusters below that critical radius become nucleation points for β'' phase, while the ones above that radius coarse and contribute to the yield strength of the material. The target of this procedure is Bimodal Precipitate Structure which includes dense and small precipitates but also large, coarse and strong ones, a mix that improves the mechanical properties of the alloy. The advantages of 2-step aging over the standard solution treatment and single step aging are that the maximum strength and hardness are increased, the overall time of aging is reduced, and the energy required for attaining the results is smaller.

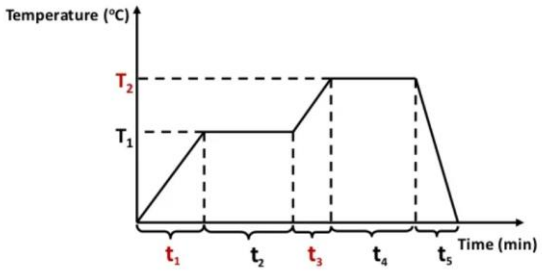

Figure 5: Qualitative double T5 aging diagram

1.3 Mg_2Si Precipitation

1.3.1 Nucleation of pre-β'' phase

The single most important transformation in aging of 6xxx aluminum alloys in general is the precipitation of Mg_2Si, something that applies to the 6060 alloy of this study. This intermetallic phase undergoes a transformation 3 times before the most stable form is reached. The transformation path is pre-β''→ β''→β'→β. This procedure is targeted to stop in between the transformation from β'' to β', as studies have shown that the best results regarding strength and hardness, are achieved from β'' phase. These results are backed up by the theoretic conclusion regarding the hardness/strength to particle radius diagram below. The optimum results are achieved right before coherency loss which in our sequence of transformations happens right before β' phase is achieved. Total loss of coherency would be detrimental, as the Orowan mechanism would be easily activated, and plastic deformation would destroy the material.

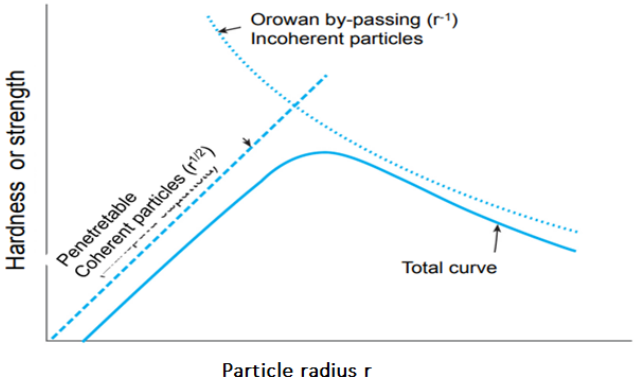

Figure 6: Hardening by penetratable and non-penetratale particles as a function of particle size (aging time).[4]

The pre-β'' phase is the first that forms. It is a metastable intermetallic phase and forms during quenching from solution temperature and at the first stages of aging. Its nucleation is heterogeneous, as it first shows up filling vacancies of the supersaturated solid state, which are imperfections of the matrix. It also nucleates from the smaller co-clusters formed during quenching and at the dislocations of the matrix. Although the driving force for nucleation of β phase is bigger, the energy barrier of pre-β'' and each consecutive phase after it is lower. That is the reason that the sequence of transformations happens and β phase is not directly

formed. Pre-β''particles are needle-like shaped and derive from the substitution of Al in the matrix with Mg and Si. Thus, the precipitation is limited near the grain boundaries and Precipitation Free Zones are introduced to the material. This unwanted effect can be mitigated by two-step aging, where a bigger dispersion of finer precipitates is achieved. The phase's early stages can be perceived as Mg-Si dimmers that slightly deform the Al matrix. In order for the pre-β'' to be established at a certain place into the lattice, a lot of dimmers have to gather at this area, therefore it becomes of high constitution in solute atoms and is considered a precipitate. These particles are highly coherent with the Al matrix, though not entirely. Particle size is still into the order of nanometers and its atomic structure resembles this of the co-clusters, albeit the shape.

1.3.2 Growth and formation of β''phase

After the nucleation of pre-β'' phase, the transformation to the main strengthening phase of 6xxx aluminum alloys, β", starts. This is a diffusional heat activated mechanism. The speed of the transformation is determined by diffusional control, as the Mg and Si atoms precipitate from the supersaturated solid portions of the matrix. The interface in semi-coherent, and during the transformation it becomes less coherent. The type of interface suggests that mobility is high, and the speed is regulated by the atoms passing the interface. As suggested in [1], the growth speed is given by the equation:

$$u = \frac{\Omega}{2}\sqrt{\frac{D}{t}}$$

whereas Ω is the supersaturation factor:

$$\Omega = \frac{C_0 - C_a}{C_\beta - C_a}$$

C_o the alloy constitution, C_β the Mg_2Si constitution and C_a the constitution after the precipitation and D the diffusion coefficient.

In order to achieve β'' phase, the diffusion has to stop before reaching the equilibrium state, as then, the particles would have transformed into β phase. Moreover, excessive coarsening of the particles has to be avoided, as the dispersion and the strengthening effect is reduced.

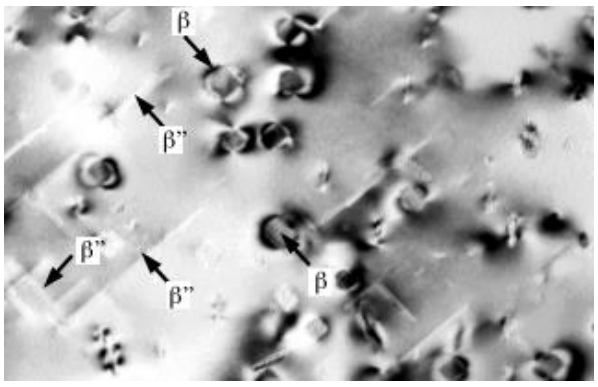

Figure 7: β" Mg2Si Microscopy, 100nm, provided by SINTEF

Coarsening, except from reducing strength, induces the PFZ's problem. The finer precipitates that reach closer to the grain boundaries are dissoluted. Coarsening speed is increased rapidly with temperature, so it is crucial to avoid over-aging 6xxx aluminum alloys. According to Lifshitz's, Solyov's and Wagner's LSW theory, the coarsing kinetics are described by the equation:

$$r^3 - r_0^3 = \frac{8D\gamma v_m C_\infty}{9kT} t$$

where r_0^3 is the mean dispersion radius before coarsening. It is deduced that the kinetics of coarsening are controlled by the diffusion coefficient D and the dominant phase constitution C_{00}. These factors increase exponentially with temperature and so does the particle radius. The driving force for coarsening is the reducing of interfacial energy. The particles radius of curvature as suggested by Gibbs- Thompson effect, is given by the type:

$$\Delta G = \frac{2\gamma V_m}{r}$$

where V_m is the molecular volume of Mg_2Si phase, r is the radius of curvature and γ is the interfacial energy. This suggests that the needle-like shaped β'' particles will have a very high interfacial energy as they have a big curvature radius. Extended coarsening will start to occur if heat treatment continues, so once more is proved that the time at which aging ends, is crucial for the final mechanical properties of the material.

2. Methodology

2.1 TC-Prisma and KWN model

The main body of this research was conducted using the TC-Prisma model for replicating the precipitation during aging of the 6060 Aluminium alloy. That model utilizes the Kampmann-Wagner Numerical method (KWN) [5,6] in order to provide the user with usable simulation data for the nucleation, growth and coarsening of precipitates in various alloys with several phases. The aim of using the KWN model is to provide industry and researchers with a solid way of predicting the precipitation that happens during aging or homogenization accurately and thus help determine the resulting microstructural and mechanical properties after the heat treatment process. In the present study the KWN model implemented in TC-Prisma was used to model the precipitation kinetics of needle like β'' particles in a 6060 Al alloy during extrusion cooling, followed by a two-step aging heat treatment. The results are then used to determine the evolution of the yield strength during heat treatment and model the stress-strain response in tension using a constitutive model as discussed in the following paragraphs.

The KWN model is the evolution of the modified form (MLS) of the Langer-Schwartz model (LS) [7]. This model relies on solving a plethora of rate equations combined with the particle size distribution function (PSD). The modification in comparison to the original LS model is

that the MLS takes into consideration the Gibbs-Thomson equations for the solubility of small particles. The results are more accurate as the original LS depends on simplistic assumptions for the nucleation and growth rate of the particles. The KWN model, improves upon the previous models by directly solving the continuity equation of PSD instead of considering only the mean radius and particle density. According to the TC-Prisma manual[5], a summary of the KWN model implementation into the precipitation module, could be described by the schematic presented in Figure 3.

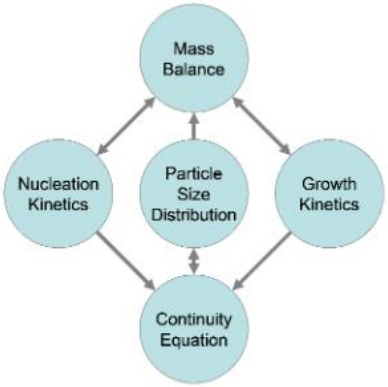

Figure 8: Schematic representation of the KWN model as implemented in TC-Prisma

A short description of the KWN model is discussed as follows. The nucleation rate of Mg_2Si or metastable β'' precipitates can be described from the Becker-Doring theory [2,5 8] , an evolution of classic nucleation theory, which considers the incubation period and produces the nucleation rate:

$$J(t) = N_0 Z \beta^* exp\left(-\frac{\Delta G^*}{kT}\right) exp\left(-\frac{\tau}{t}\right)$$

where N_0 is the total number of nucleation sites, T is the absolute temperature, t is time, Z is the Zeldovich factor:

$$Z = \frac{V_m^\beta}{2\pi N_A r^{*2}} \sqrt{\frac{\gamma}{kT}}$$

k is the Boltzmann constant, γ is the interfacial energy, V_m^β is the molar volume and N_A the Avogadro's constant. Parameters $\beta^*, \Delta G^*$and τ are defined as follows:

β^*, the atomic or molecular attachment rate is the rate at which new atoms are added to the nucleus (mass transport during nucleation) and is given by

$$\beta^* = \frac{4\pi r^{*2}}{a^4}\left[\sum_{i=1}^{k} \frac{\left(X_i^{\beta/\alpha} - X_i^{a/\beta}\right)^2}{X_i^{a/\beta} D_i}\right]^{-1}$$

Where r^* is the critical radius for nucleation, $\mathbf{X_i}$ are the respective mole fractions of element i at the interface in the precipitate and the matrix, $\mathbf{D_i}$ is the diffusion coefficient and α is the lattice parameter. The energy barrier for nucleation (Gibbs activation energy) is given by

$$\Delta G^* = \frac{16\pi\gamma^3}{3\left(\Delta G_m^{a\to\beta} / V_m^{\beta}\right)^2}$$

where γ is the nucleus/matrix interfacial energy, V_m^{β} the molar volume of the precipitate and $\Delta G_m^{a\to\beta}$ is the molar Gibbs energy for precipitation of the β phase in the α matrix, i.e the maximum driving force for the $a \to \beta$ transformation. The incubation time τ for an isothermal reaction is the time needed to achieve steady-state nucleation conditions and is given by

$$\tau = \frac{1}{\theta\beta^* Z^2}$$

where θ differs through every derivation, but a value of $\vartheta=2$ is adopted in the PRISMA software.

Finally, the critical radius for nucleation is provided as a function of supersaturation according to the thermodynamics

$$r^* = -\frac{2\gamma V_m^{\beta}}{\Delta G_m^{a\to\beta}}$$

where the interface composition is taken equal to the mean composition in the matrix.

The calculations were conducted under the general growth model of the PRISMA module which corresponded better to the specific requirements of the case study.

The growth/dissolution rate can be calculated by solving the one-dimensional diffusion equation (LaPlace) in the radial ® direction for spherical precipitates, in a pseudo-steady state approximation, assuming a constant diffusion coefficient and assumption that the alloy is dilute enough so that the diffusion fields between particles do not overlap:

$$v = \frac{K}{r}\left[\Delta G_m - \frac{2\gamma V_m^{\beta}}{r}\right] = \frac{2\gamma V_m^B K}{r}\left[\frac{1}{r^*} - \frac{1}{r}\right]$$

where the kinetic parameter K is defined as

$$K = K_{sphere}^{general} = \frac{1}{(\Delta X^{a\beta})\left[\ddot{G}\right][D]^{-1}[\Delta X^{a\beta})}$$

with $\left(\boldsymbol{\Delta X^{a\beta}}\right]$ and $[\boldsymbol{\Delta X^{a\beta}})$ being row and column vectors respectively that contain composition differences, $\left[\ddot{\boldsymbol{G}}\right]$ the corrected thermodynamic factor matrix and $[\boldsymbol{D}]^{-1}$ is the inverse of the chemical diffusivity matrix.

Finally, coarsening is considered through the growth equation by incorporating the chemical diffusivity matrix $[\boldsymbol{D}]$ into the kinetic parameter K. The matrix contains information for the

chemical potentials for the far-field matrix composition and for the equilibrium composition. It comprises that information in the form of an arithmetic mean of the diffusivity along the material. Regarding the growth/dissolution events, particles with $r > r^*$ will grow and particles with $r < r^*$will shrink. To account for non-spherical particle growth, as in the case of needle like β'' particles, the kinetic factor K is modified based on a prefactor calculated in terms of the aspect ratio of the particles.

In the current study, the values for the above parameters corresponding to PRISMA module are:

- ΔG^*=-3500 KJ is the Gibbs energy addition for the nucleation to happen
- $Needle\ aspect\ ratio = 10$ for the β'' particles
- Interfacial energy prefactor = 0.65
- Bulk nucleation model is considered

The model of the continuity equation used by PRISMA module [5] is expressed as:

$$N = \int_0^\infty f(x)\,dr$$

$$\langle r \rangle = \int_0^\infty r f(r)\,dr$$

$$\phi = \int_0^\infty \left(\frac{4\pi}{3}\right) r^3 f(r)\,dr$$

where $f(r)$ is the Particle size distribution of a precipitate phase, N the number of particles per unit volume $\langle r \rangle$ the mean radius and ϕ the particle volume fraction. The evolution of $f(r)$ in time follows the continuity model presented by Langer and Schwartz in [7]:

$$\frac{\partial f}{\partial t} = -\frac{\partial}{\partial r}[u(r)f(r)] + j(r)$$

where $u(r)$ is the growth rate of an r sized particle and $j(r)$ is the distributed nucleation rate, defined by the nucleation rate equation:

$$J = \int_{r^*}^\infty j(r)\,dr$$

2.2 Modeling of mechanical properties

2.2.1 Kocks-Mecking-Estrin (KME) Equation

As a complimentary addition to the previous work on the aged aluminium alloys, an effort was made to construct a constitutive model in MATLAB that could predict the tensile behaviour of the alloy, provided some experimental measurements and parameters. The flow stress of an alloy is closely related to the dislocation density evolution due to forest hardening during plastic deformation. The dislocation density, can be calculated by taking into account the dislocation interactions with other dislocations and various other obstacles

impeding their motion during deformation, according to the Kocks-Mecking-Estrin (KME) equation:

$$\frac{d\rho}{d\varepsilon} = \frac{M}{b}\left[\frac{k_3}{\lambda_p} + \frac{1}{D_{gb}} + k_1\sqrt{\rho} - k_2 b\rho\right]$$

Where ρ is the dislocation density, ε is the true strain, b the Burgers vector, M the Taylor factor, D_{gb} the grain diameter, λ_p is the average spacing of strengthening precipitates as given by Lee et.al [9]:

$$\lambda_p = \frac{d_{vc}}{\sqrt{f_{vc}}}$$

where d_{vc} is the average precipitate diameter and f_{vc} is the volume fraction of the precipitates, k_1 is the dislocation generation factor, k_2 the dislocation annihilation factor and k_3 the dislocation-precipitate interaction effectiveness factor. The k_i factors are considered as the main calibration parameters of the constitutive model to determine the evolution of the true flow stress during deformation. The first two terms in the KME equation account for workhardening due to an interaction of dislocations with unshearable strengthening precipitates and grain boundaries respectively, increasing the dislocation density. The last two terms account for dislocation self-interactions generating and eliminating dislocations dynamically during deformation. By numerically solving the KME equation, we obtain the dislocation density referring to strain and utilise it to produce the predictive stress-strain diagram.

2.2.2 Flow stress model

To estimate the complete flow stress behavior of the material the following equation is used:

$$\sigma = \sigma_{ss} + \sigma_{GB} + \sigma_{pr} + \sigma_{\rho}$$

where σ_{ss} is the solid solution strengthening which for our case is considered constant, σ_{GB} is the grain boundary strengthening which derives from the Hall – Petch equation:

$$\sigma_{GB} = \frac{K_{HP}}{\sqrt{D_{GB}}}$$

where K_{HP} is the Hall-Petch strengthening coefficient.

The precipitation hardening contribution σ_{pr} is obtained using the following set of equations from Zander et.al[10]:

$$\sigma_{pr} = \frac{M}{b}\sqrt{\frac{3f}{2\pi}}(2\beta G b^2)\left(\frac{1}{r_C}\right)^{\frac{3}{2}}\sqrt{\bar{r}} \quad , \quad r < r_C$$

$$\sigma_{pr} = \frac{M}{b}\sqrt{\frac{3f}{2\pi}}(2\beta G b^2)\frac{1}{\bar{r}} \quad , \qquad r \geq r_C$$

where f is the volume fraction of the precipitates, β=0.36, G (or μ) is the shear modulus, r_c the critical precipitate size and $\bar{r}$ the mean precipitate size (the rest as seen above).

σ_ρ is the dislocation density forest hardening, accounting for the evolution of the yield stress (flow stress) as a function of strain, during plastic deformation:

$$\sigma_\rho = a_\rho M \mu b \sqrt{\rho}$$

where α_ρ is equal to 0.3 – 0.4, μ is the shear modulus and ρ is the dislocation density. The dislocation density depends on the strain of the material, and it is the outcome of the Knocks-Mecking-Estring equation. For the initial ρ_0 value as well as the values of the solid solution strengthening σ_{ss} and the Hall-Petch coefficient K_{HP}, we compute the σ_y of the material so that it is close to the experimentally observed value.

The model was fitted to uniaxial tension stress-strain data regarding four processing stages, the as cast, homogenized, extruded and aged stages. Then, the engineering stress-strain data were transformed to true quantities for a direct correlation between the model and the experiment, using the following set of equations:

$$\varepsilon_{tr} = \ln(\varepsilon_{eng} + 1)$$

$$\sigma_{tr} = \sigma_{eng}(1 + \varepsilon_{eng})$$

Samples from the experimental stress-strain data were drown in order to make the fitting and the calculations easier and faster to complete, as well as to exclude the elastic strain and the necking phase of the test because the model can only describe the evolution of stress in the uniform plastic regime. A variable n is inserted into the model, which determines the intervals at between the data are selected.

After the experimental data are sorted, the model can be fitted by minimizing the error between the calculated values and the experimental. In order to do this, the k_i factors of the Kocks-Mecking-Estrin model are initially estimated values and then adjusted systematically, to minimize the error. This allows us to estimate the dislocation density throughout the workhardening stage of the material.

The precipitation hardening particles are assumed spherical, with a radius equal to the needle radius, for the calculation of their contribution to the initial yield strength of the material. When the radius is small, particles are shearable by mobile dislocations, whereas as the radius increases above a critical radius, the Orowan mechanism takes effect and dislocations bow around the particles. In order to differentiate and project the contribution of the precipitates on the initial yield stress, we need to calculate the contribution for radii smaller and larger than the critical radius.

When the first set of estimated strength and workhardening values is obtained, we select between mean absolute error or mean squared error and produce each value using the following set of equations:

$$Mean\ Absolute\ Error\ (MAE) = \frac{1}{N}\sum_{i=1}^{N}\left|\sigma_i^{exp} - \sigma_i^{num}\right|$$

$$Mean\ Squared\ Error\ (MSE) = \frac{1}{N}\sum_{i=1}^{N}\left(\sigma_i^{exp} - \sigma_i^{num}\right)^2$$

Then, using the fmincon minimization algorithm in Matlab (gradient-based algorithm for constraint non-linear functions) we find the optimal values for the constants k1, k1 and k3 by minimizing the corresponding mean error of our choice. This way, we obtain the best correlation between real and projected values and minimizing the errors between the stress-strain diagrams.

After the experimental data are transformed and sampled down and the k_i parameters are optimized, we apply the Kocks-Mecking-Estrin model with the optimal values for the k factors that are obtained from the minimization algorithm. With these calculations at hand, we can then extract the final contribution to strengthening as well as the workhardening rate.

The model can be applied to any type of aluminum, provided that every required measurement is given and the prior manipulation if the material is documented precisely.

3. Experimental Results

3.1 Characterization of materials

3.1.1 As Extruded material

The as extruded material was studied experimentally by SINTEF, and the microstructure was characterized via SEM-EDX analysis. The aim of the analysis was to identify the phases present after extrusion cooling and determine the presence of undesired microstructural features. More specifically, the growth of β − Mg_2Si, or other β-family metastable precipitates, on preexisting α-AlFeSi and Dispersoid ($Al_{15}Si_2M_4$) particles, during extrusion cooling was studied. Additionally, the matrix and particle composition were also measured, to provide information regarding the supersaturation of Mg and Si the matrix, prior to aging.

During extrusion cooling, the key sites for nucleation of β-family metastable precipitates are preexisting α-AlFeSi particles, dispersoids and grain boundaries. The possible nucleation particles are β'', β', β, B', U1, U2 and the unwanted in this instance β-Mg_2Si. During the nucleation of these particles, precaution should be taken in order to minimize the formation of Precipitation Free Zones (PFZ) which lead to degraded ductility during aging. β-Mg_2Si was studied by SEM EDX analysis while the PFZ's and metastable particles of aged material by TEM analysis, all conducted by SINTEF. Microstructure analysis of as extruded material is presented in Figure 9 through Back Scattered Electron (BSE) mode of SEM analysis. The bright areas of Figure 9 are identified as iron (Fe) intermetallics, remnants of homogenization.

EDX analysis concluded that the only intermetallics present after extrusion cooling are α-AlFeSi phase and dispersoids. The spherical particles observed in Figure 9 are the result of heat and deformation during extrusion. No equilibrium $\beta - Mg_2Si$ was detected in the BSE-SEM images of the as extruded material (dark particles) in BSE mode. This indicates that any $\beta - Mg_2Si$ particles that remained from solidification were completely dissolved in the matrix and that reprecipitation of this phase did not occur. This is in-line with EDX measurements of the chemical composition of the aluminum matrix, as shown in Spectrum 14 of Figure 9 d), where the average Mg concentration measured, is very close to the nominal concentration in the alloy. The Si content of the matrix was inconclusive, though it is expected to be lower than the nominal since Si is bounded in α-AlFeSi and Dispersoids. The aluminum matrix is supersaturated in Mg and Si, resulting in an increased driving force for precipitation of β-family strengthening particles like β′′. In the case that significant fractions of $\beta - Mg_2Si$, or other Mg containing precipitate like π-phase, β′′, β′, B′, U1 or U2, were formed during extrusion cooling, the Mg content in the aluminum matrix would be lower than the nominal. Yet very fine, metastable precipitates with very low volume fraction might be present after extrusion. The observation of metastable precipitates like β′′, β′, B′, U1 or U2, on α-AlFeSi, Dispersoids and grain boundaries requires Transmission Electron Microscopy and was performed in the aged material, discussed in section 3.1.2.

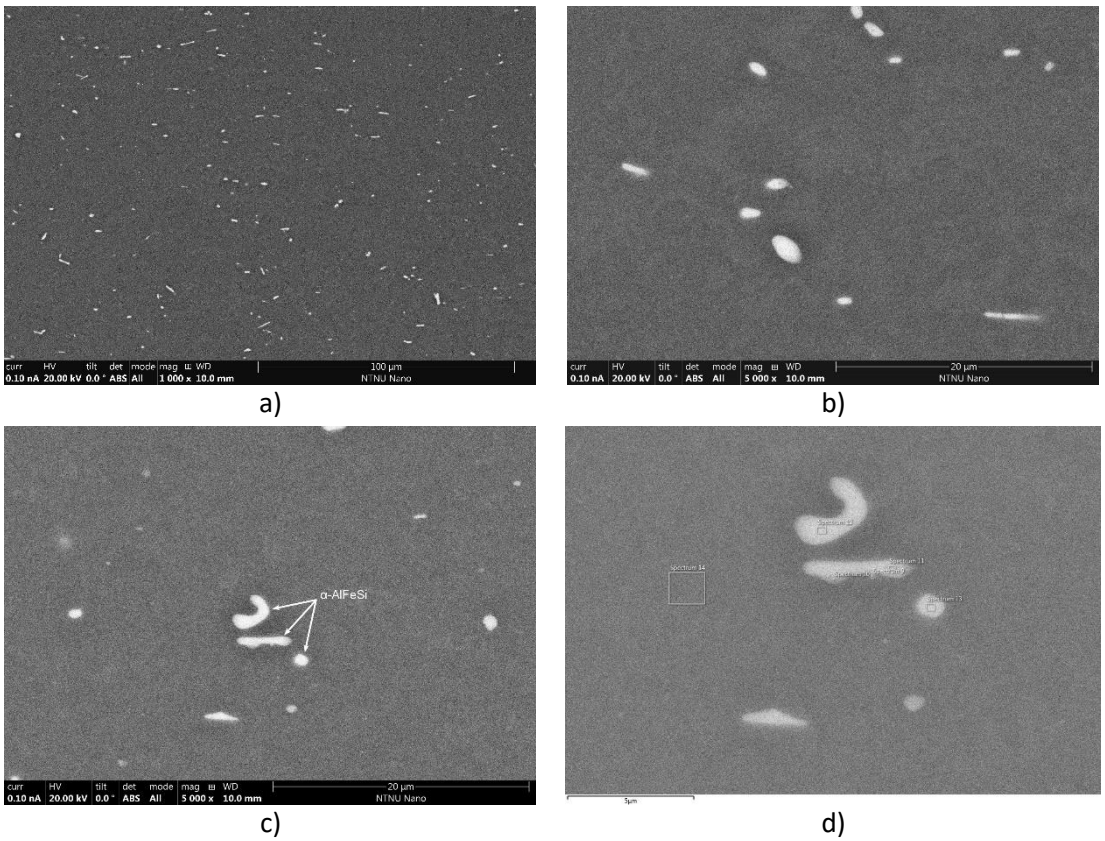

Figure 9: SEM micrographs of the as extruded material using Back Scattered Electron (BSE) mode. The location of the EDX measurements is shown in d). Images and measurements as provided by SINTEF.

3.1.2 Aged material

The material after extrusion and aging, was examined via Transmission Electron Microscopy, to determine the structure and morphology of the strengthening precipitates, as well as to examine the presence of overaging particles, growing on α-AlFeSi, dispersoids and grain boundaries. Finally, the width of the Precipitate Free Zones (PFZs) around dispersoids and grain boundaries was measured. The TEM analysis was performed by SINTEF in aged specimens along the aluminum direction, after preparation using standard twin jet electropolishing technique.

The TEM results are summarized in Figure 10, where Bright and Dark Field are presented in a) and b), along with high magnification images of the cross-section of the strengthening precipitates, which were identified as β′′. The β′′ needles grow in length preferentially along the aluminum directions [11–13], thus in order observe the cross-sectional area of the precipitates, the aged material was examined along the direction. The growth of needles along the three perpendicular directions, is evident in the Bright and Dark Field images of Figure 10 a) and b) respectively. Based on the morphology of the needles presented in Figure 10, it is concluded that the strengthening phase is the metastable β′′- $Mg_5Al_2Si_4$. This is evident by the characteristic monoclinic unit cell of β′′-$Mg_5Al_2Si_4$, as shown in Figure 10 c) and d). The β′′- $Mg_5Al_2Si_4$, needles are fully coherent with the aluminum matrix.

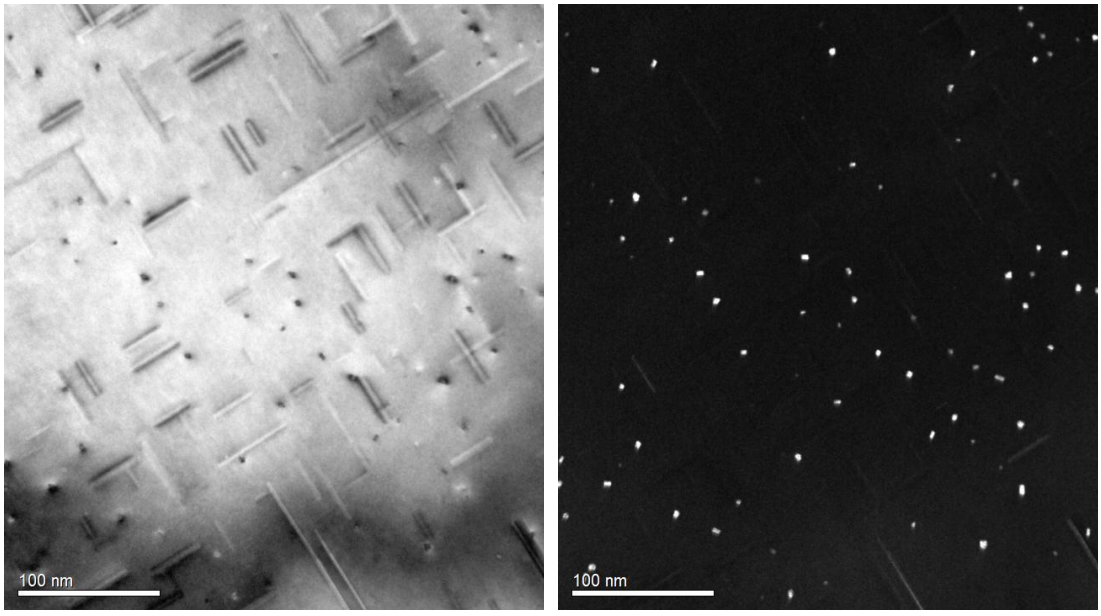

a) b)

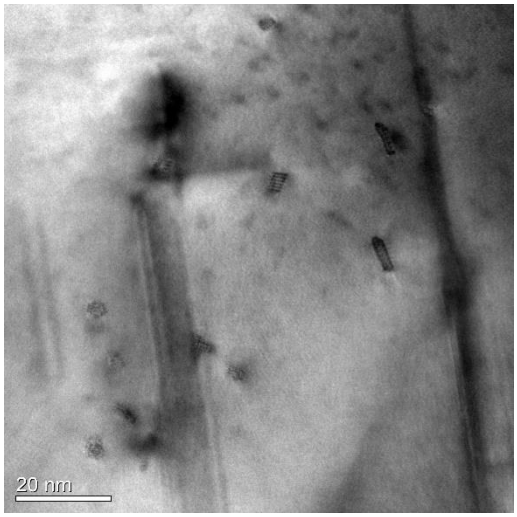

c)

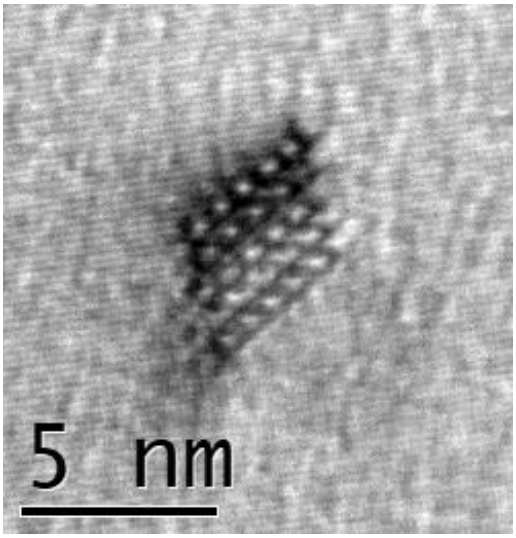

d)

Figure 10: TEM micrographs of the aged material showing the θ'' strengthening precipitates. Bright and dark field images are presented in a) and b) along with high magnification images of the θ'' cross-sections in c) and d). Images as provided by SINTEF.

The distribution of β''-$Mg_5Al_2Si_4$ particles was quantified by image analysis of the TEM micrographs. More specifically, the distributions of the needle particle length and cross-sectional area were measured using low magnification Bright Field images as shown in Figure 10 a). To measure the average number density of precipitates (# of particles per unit volume), Dark Field TEM micrographs were used, presenting higher contrast for the needle cross-sections, as shown in Figure 10 b). To accurately determine the number density, the specimen thickness is required, which was measured with high precision via the 2-Beam CBED technique. Then by multiplying the average precipitate volume and the number density, the volume fraction of precipitates can be determined. The distributions of needle cross-sectional area and length are presented in Figure 11 a) and b) respectively. When observing Figure 11, it is obvious that the majority of the particles have a cross sectional area between 8 and 16 nm^2, averaging at $\bar{A} = 12.3$ nm^2. The same applies to needle length which averages at $\bar{L} = 40\ nm$, with the majority of particles between 15 and 50 nm. These measurements cannot be correlated because they are extracted from different particles courtesy to TEM limitations. Though, it is logical to attribute them to similar particles. Finally, the volume fraction of the β'' precipitates was measured to be $f_{\beta''}$ = 0.91%. Various measured values are summarized in Table 2.

Table 2: Measured θ'' particle properties after aging. Measurements provided by SINTEF.

Measurement	$\bar{A}(nm^2)$	$\bar{L}(nm)$	$\bar{r}_d(nm)$	AR	$N(m^{-3})$	$f_{\beta''}(\%)$
Value	12.3	40	2.83	7	1.85 10^{22}	0.91

The TEM measurements provided, show that the material has undergone a very good aging procedure that exploits the max potential of metastable strengthening precipitate particles.

The high volume fraction and number density of β'' needles indicates that a fine particle dispersion is achieved. The Al matrix is no longer supersaturated in Mg and Si, and the β'' particles are fully coherent with it. Although the needle length is rather large according to previous studies, most particles are shearable and contribute to coherency hardening due to the small radius of the needles. TEM analysis revealed that there were no overaging precipitates (β',B',U1,U2 or β-Mg_2Si) present in the material and that the overall condition is slightly underaged and very close to peak hardness. Said peak hardness has been measured when the material is aged right on the edge of coherency loss, before the Orowan mechanism takes effect. Some overaging particles were found around dispersoids and in grain boundaries but the can be attributed to PFZs creation caused by slow extrusion cooling [15–17].

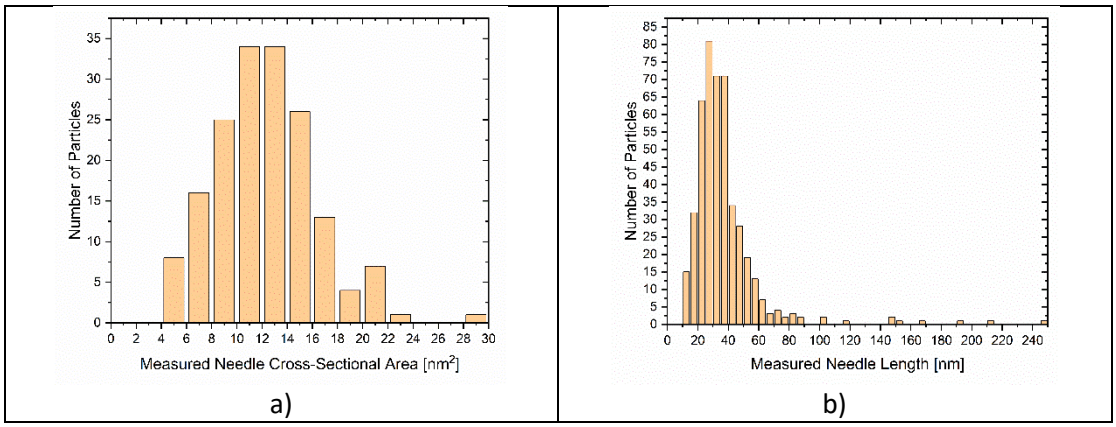

Figure 11: Distributions of β'' needle a) cross-sectional area and b) length as measured by image processing of TEM micrographs. All measurements provided by SINTEF.

Precipitate Free Zones (PFZs) were observed around dispersoid particles and near grain boundaries as presented in Figure 12 and 13 respectively. The PFZs are regions of the material where precipitation of the strengthening β'' phase has not occurred during aging and are associated with decreased ductility. Many dispersoids are attached to overaging precipitates on the boundaries with the Al-Matrix, as shown in Figure 12 c) and d). The average width of the grain boundary PFZs is increased compared to that of the dispersoids. Dispersoids formed during homogenization and coarse overaging precipitates, nucleating during extrusion cooling and growing during aging, were also found along the grain boundaries as presented in Figure 12 b). The characteristics of PFZ around dispersoids and grain boundaries are roughly the same, albeit the effects are more intense around grain boundaries as diffusion is accelerated there. As TEM measurements concluded, the rather large PFZs of this material might decrease the elongation if the aged material by inducing void nucleation and growth at these areas. This leads to reduced ductility and premature failures.

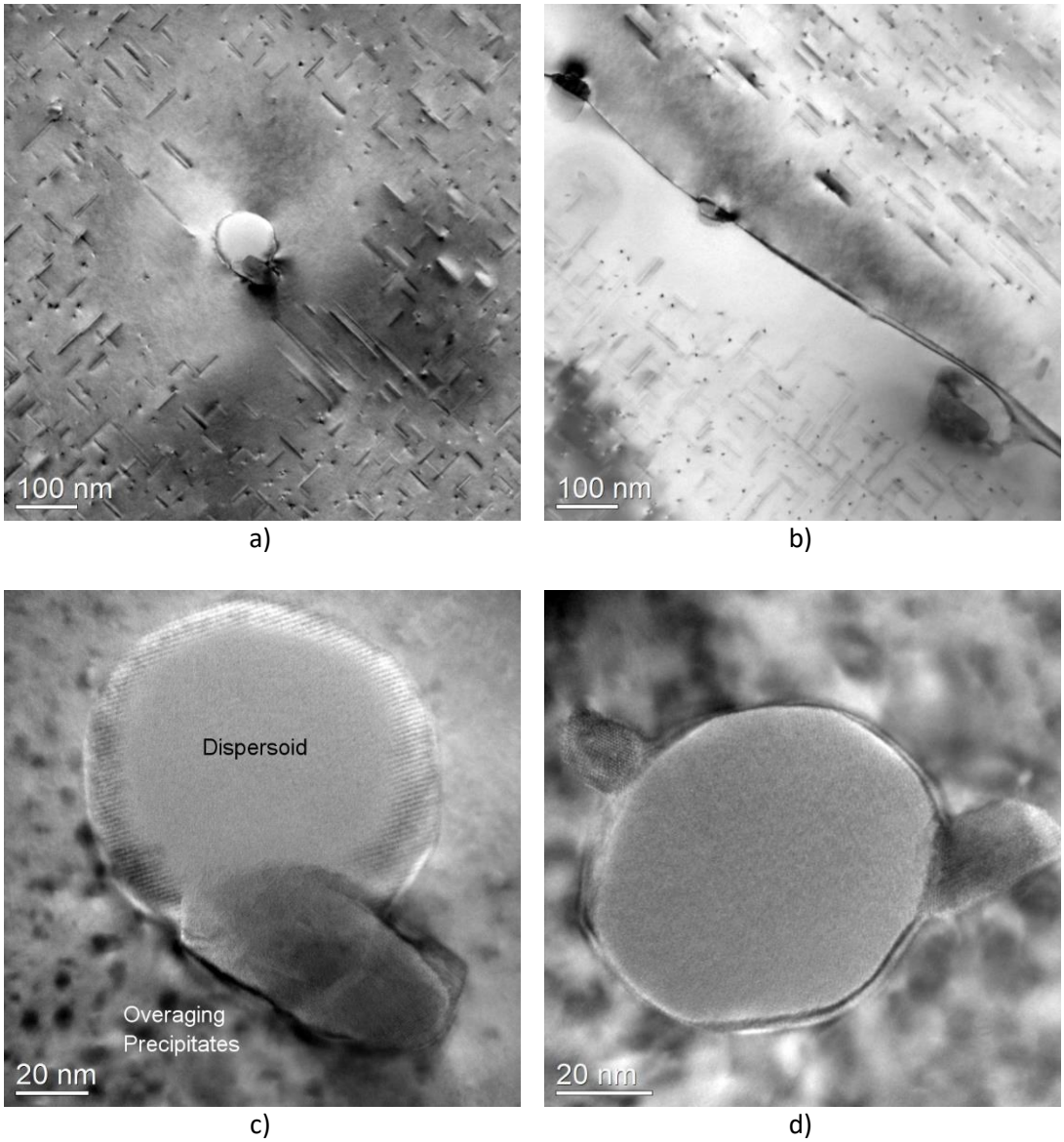

Figure 12: TEM micrographs of the aged material showing the Precipitate Free Zones (PFZs) in a) & b) and the overaging precipitates around dispersoid particles in c) & d). Images as provided by SINTEF.

The coarse overaging precipitates, formed on dispersoid particles and grain boundaries are presented in the high-resolution TEM micrographs of Figure 13. The overaging particles are comprised of a mixture of different metastable phases in the β-Mg_2Si family, each with a distinct crystal structure. Under close examination several metastable phases were identified, based on their crystal structure and shape. Finally, a disordered particles of the β-family were also found though it was not possible to be further characterized. The TEM images of those particles are presented in Figure 13.

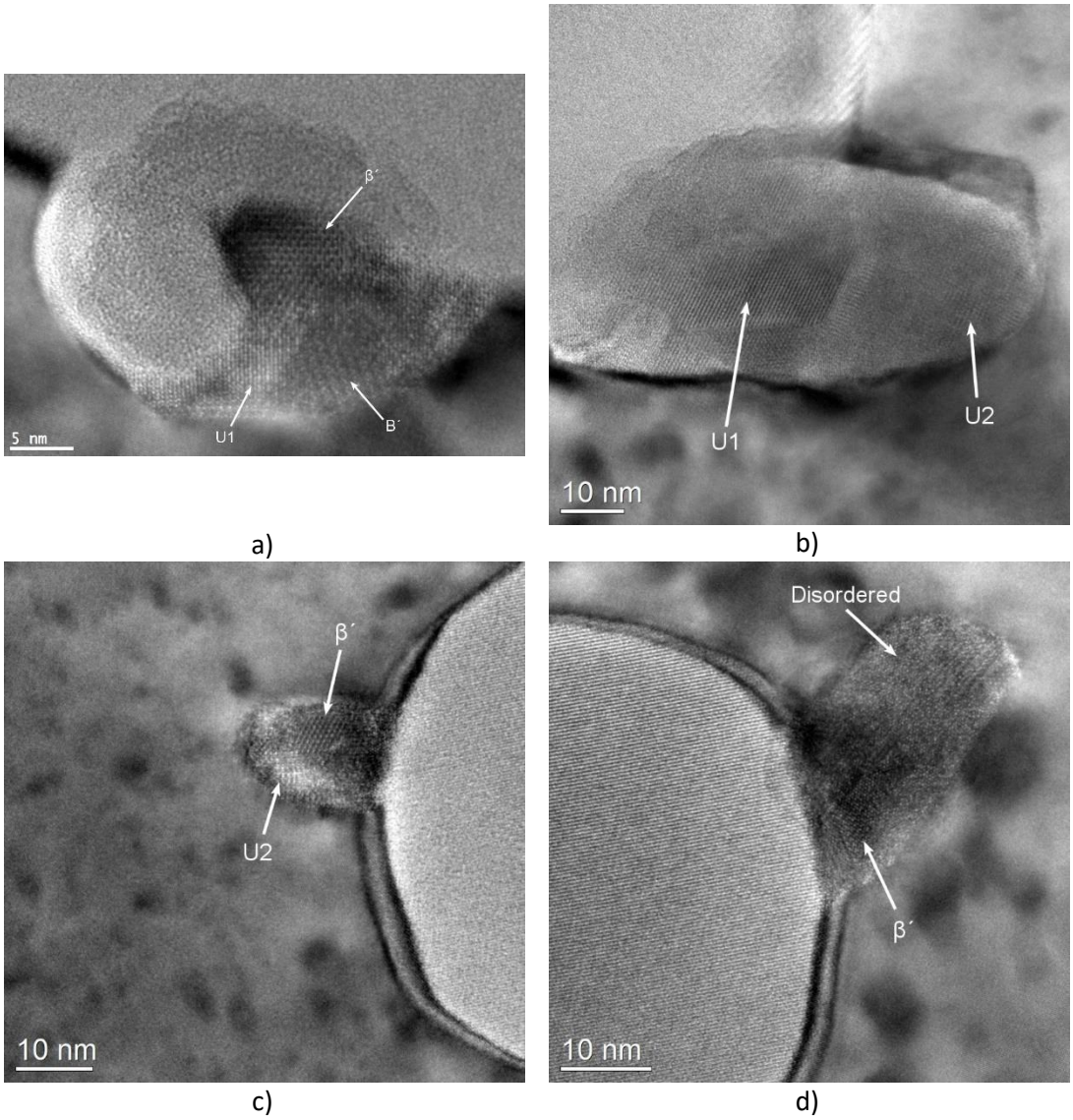

Figure 13: TEM micrographs of the overaging precipitates forming around dispersoid particles in the aged material. A mixture of β´, U1, U2, B´ and disordered phases can be observed. Images as provided by SINTEF.

The aforementioned PFZs are formed mainly because of the temperature driven solid-state diffusion mechanism. During extrusion cooling vacancies and solute atoms like Mg and Si are driven from their matrix position closer to dispersoids and grain boundaries, i.e nucleation points. A zone around these areas is depleted from these elements, and subsequently deprived of its nucleation sites. Thus, away from dispersoids and grain boundaries where vacancies and solute atoms are gathered nucleation does not happen and the nuclei on the interfaces are very small due to temperature continuously dropping and diffusion stops. During aging when diffusion starts again, a fine dispersion of β'' metastable particles is created in the bulk material, but this is not reflected in the zones mentioned previously. This is a result of the matrix not being supersaturated of Mg and Si and of the nucleation sites migrating near the interfaces. Concurrently, the big precipitates on the interfaces and mainly on grain boundaries tend to become very large and promote the formation of overaging particles. To mitigate the development of PFZs and overaging precipitate clusters, a higher

extrusion cooling rate should be used, in order to hinder the migration of vacancies and solute atoms to the interface, by limiting diffusion.

3.2 Tensile Testing

Uniaxial tensile testing at room temperature was conducted by the Laboratory of Mechanics and Strength of Materials at the University of Thessaly, in both smooth and notched specimens of the as cast, homogenized, as extruded and aged materials. In the case of the as extruded and aged materials, rectangular specimens were machined along the extrusion direction, from the provided profile sections, according to the ASTM E8M specification. To study the effect of stress triaxiality on the mechanical response of the material, a 2mm radius notched was machined in the notched specimens. A schematic representation of the dimensions and geometry of the rectangular tensile specimens is presented in Figure 14, along with the experimental setup in the uniaxial tension machine.

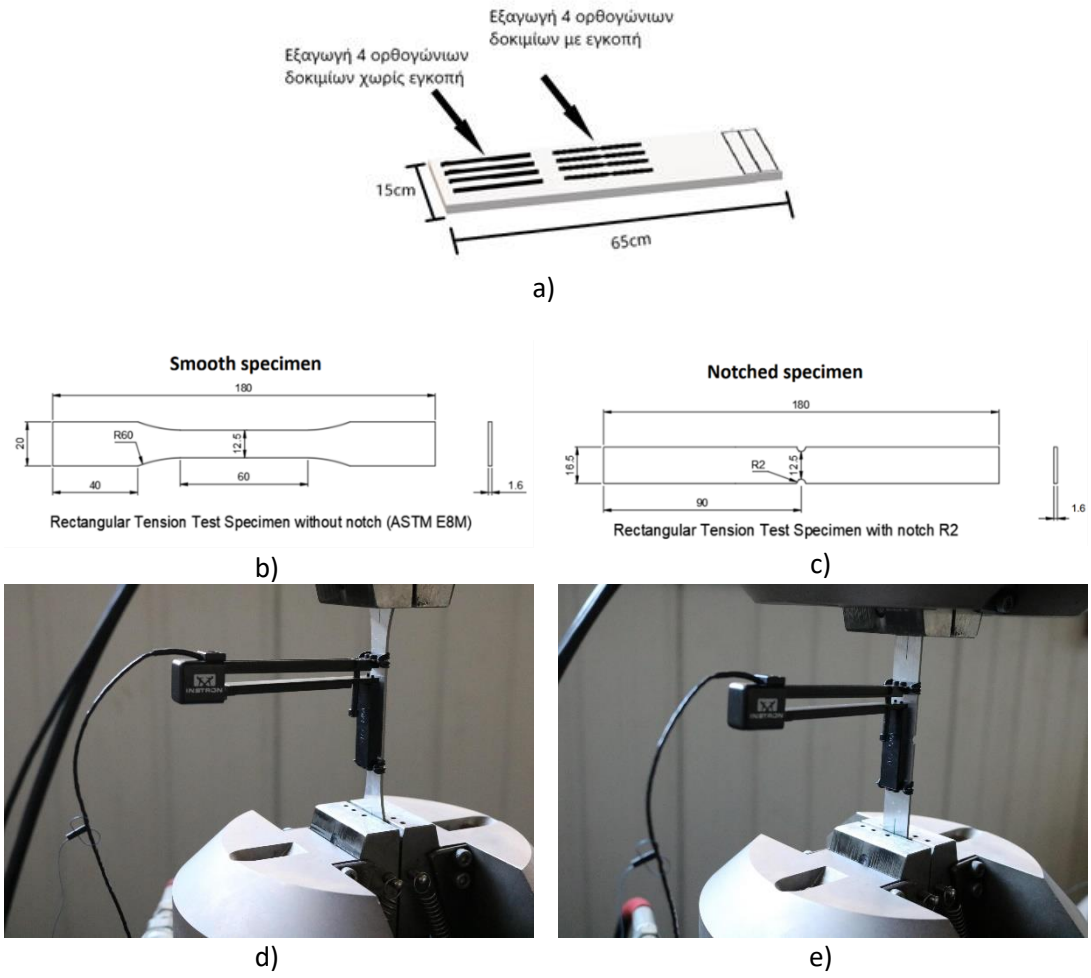

Figure 14: Schematic representation of the smooth and notched rectangular tensile specimens, of the as extruded and aged materials, along with photos of the experimental setup. Images as provided by Laboratory of Mechanics and Strength of Materials, University of Thessaly.

3.2.1 Smooth Specimens Tensile Testing

The smooth tensile test specimens of the as cast, homogenized, as extruded and aged materials, were subjected to uniaxial tension until fracture. The yield strength was measured as the stress at 0.2% strain, for all materials. The aged condition presents considerably increased yield strength, due to the precipitation of a very fine dispersion of β'' needles. Similar trends can be observed in the engineering ultimate tensile strength (UTS), where localized plastic deformation occurs, as a neck in the specimens forms. The formation of the neck indicates the end of the uniform plastic flow, and the strain at which a neck forms indicates the uniform elongation, in contrast to the total strain required to fracture the material. Post uniform elongation is a measure of toughness and becomes more important when high strain rates or triaxial loading is considered. Results from the smooth specimen uniaxial tensile tests, are summarized in Table 3. The results are consistent with the observed microstructural features at each stage of processing. After extrusion not many intermetallics are present, though due to deformation, the grains have become more elongated and some β-family particles have precipitated upon cooling, raising strength and lowering elongation. Finally, in the aged condition, a very fine dispersion of β'' needle is present, resulting in a significantly increased strength and limited ductility.

Table 3: Mechanical behavior of the material, according to uniaxial tensile testing with smooth specimens. Stress and strain measurements correspond to engineering values. Measurements as provided by Laboratory of Mechanics and Strength of Materials, University of Thessaly.

Condition	$\sigma_{y_{0,2}}(MPa)$	$\sigma_{UTS}(MPa)$	$\varepsilon_{neck}(\%)$	$\varepsilon_{fract}(\%)$	$\sigma = K\varepsilon^n(MPa)$
As Extruded	70.5	165	19.7	21	$\sigma = 336.94\varepsilon^{0.2948}$
Aged	208	230	8.8	10.1	$\sigma = 296.61\varepsilon^{0.0709}$

The engineering stress-strain response of the material, upon uniaxial tensile testing with smooth specimens, is presented in Figure 15 a), whereas the logarithmic (true) stress-strain response, along with the workhardening rate is shown in Figure 15 b). Note that the workhardening rate is defined as the derivative of the true stress, as $\frac{d\sigma_{tr}}{d\varepsilon_{tr}}$. A Hollomon strain hardening relation $\sigma = K\varepsilon^n$, was fitted to the engineering stress-strain curves of Figure 16 a), as shown in the last column of Table 3. In the Hollomon relation, σ is the engineering stress in MPa, ε is the engineering strain, K is a strength constant in MPa and n is the workhardening exponent. Note that the workhardening exponent n is higher in the as cast material, whereas the aged material presents a lower value. This indicates that upon loading, workhardening is more prominent in the as extruded material. In contrast the aged material exhibits marginal increase in the flow stress as deformation progresses. This behavior is also evident in the workhardening curves of Figure 15 b), where the intersection point of the true stress with the workhardening rate denotes the theoretical point where uniform elongation stops and necking occurs. At later stages of the deformation, the workhardening rate of the as extruded material gradually drops below the others and intersects with the true stress line, as necking takes place, followed quickly by fracture. In the case of the aged material, although the flow stress is increased, the workhardening rate is high at first, decreasing rapidly until the formation of a neck and the resulting fracture, as

deformation progresses. The uniform and total elongation is reduced compared to the other materials, due to the presence of β'' needles. The width of precipitate free zones (PFZs) near dispersoids and grain boundaries, also negatively impacts the ductility of the aged material, by providing sites for void nucleation and coalescence during deformation [17].

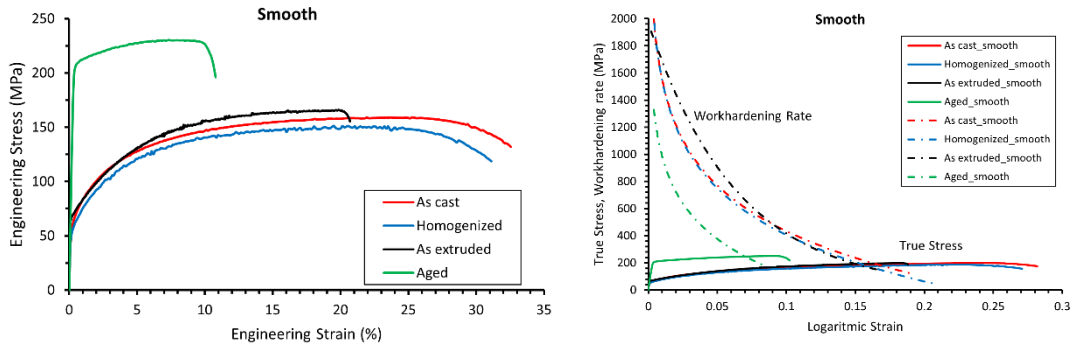

a) b)

Figure 15: a) Engineering stress as a function of engineering strain and b) true stress and workhardening rate as function of logarithmic (true) strain, upon uniaxial testing with smooth specimens. Graphs as provided by Laboratory of Mechanics and Strength of Materials, University of Thessaly.

3.2.2 Notched Specimens Tensile Testing

Tensile testing of the material at all processing conditions followed using notched specimens, in order to determine the mechanical behavior under high stress triaxiality conditions in the area of the notch. The notched experiments provide useful information for ductility under high strain rates and crash resistance. The experimental findings regarding the mechanical behavior using notched specimens are summarized in Table 4, whereas the engineering and true (logarithmic) stress-strain response, along with the workhardening rate, are presented in Figure 16. In general, the notched samples presented higher strength and lower ductility compared to the smooth specimens. The fitted Hollomon relation, presents a decreased value of the workhardening exponent n, indicating that workhardening is limited in the notched samples. This is also evident in Figure 16, where in all cases the workhardening rate rapidly decreases as deformation progresses, leading rapidly to necking and failure. Ductility is drastically reduced under the complex loading conditions near the notch, compared to simple tension.

Table 4: Mechanical behavior of the material, according to uniaxial tensile testing with notched specimens. Stress and strain measurements correspond to engineering values. Measurements as provided by Laboratory of Mechanics and Strength of Materials, University of Thessaly.

Condition	$\sigma_{y_{0,2}}(MPa)$	$\sigma_{UTS}(MPa)$	$\varepsilon_{neck}(\%)$	$\varepsilon_{fract}(\%)$	$\sigma = K\varepsilon^n(MPa)$
As Extruded	86.5	161	5.8	6.85	$\sigma = 335.02\varepsilon^{0.2579}$
Aged	227	235	0.98	1.65	$\sigma = 338.33\varepsilon^{0.0742}$

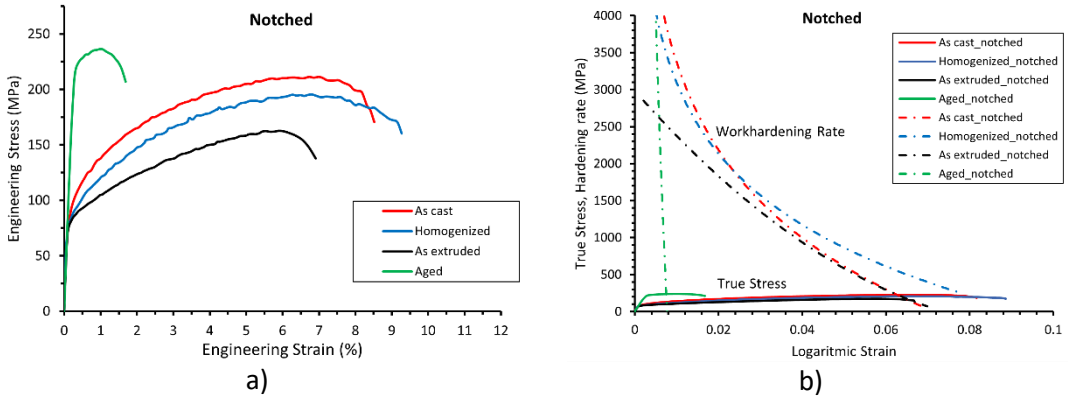

Figure 16: a) Engineering stress as a function of engineering strain and b) true stress and workhardening rate as function of logarithmic (true) strain, upon uniaxial testing with notched specimens. Graphs as provided by Laboratory of Mechanics and Strength of Materials, University of Thessaly.

4.Results

4.1 Extrusion Cooling Simulation Results

The evolution of the nucleation rate, the number density, i.e. the number of particles per unit volume, and the normalized driving force for precipitation of β'' needles during extrusion cooling with a constant cooling rate, is presented in Figure 17 a). At the start , right after extrusion, although the temperatures are relatively high, the driving force for diffusion is zero as the β'' phase is not thermodynamically stable. As the temperature decreases, we reach a spectrum where the β'' phase becomes thermodynamically stable and the β'' phase becomes thermodynamically stable and the driving force increases but there is still no nucleation of particles as the driving force is not big enough to overcome the energy barrier that occurs from interfacial and strain energy. At around 220 ^{0}C the nucleation starts and the nucleation rates spikes but shortly after returns to 0 as the temperature drops significantly in order to hinder diffusion. The number density rapidly reaches a plateau that is preserved until aging begins and diffusion commences. The result is, as shown in Figure 17, that after extrusion cooling the number density and the volume fraction of β'' precipitates is minimal.

During the first nucleation, as shown in Figure 19, the critical radius, the mean radius and the mean length of the needles start relatively high and immediately drop significantly. This happens due to the very small initial driving force and high temperatures. When the temperature drops and the driving force rises, the drop is observed. After that, a small rise is detected, as the result of the limited growth during rapid extrusion cooling. At the end of extrusion cooling these values reach a plateau for a limited period of time during the heating phase of the aging procedure. The mean radius and the mean length of the particles face a sudden drop as diffusion starts and more precipitates form in the bulk of the material, and then as growth proceeds, they steadily increase. The critical radius is maintained at the first holding temperature and at the second temperature increases as the holding starts and keeps elevating, until it is about the same as the mean radius at the end of the aging procedure. The number density distribution of particle radius and length, i.e. the number

density of particles with a specific radius and length, is presented in Figure 22, at several times throughout processing. At the end of aging procedure, the distributions of the needle length and radii are very similar, as the length is considered to be proportional to the radius, maintaining a constant aspect ratio. The current study is carried under the assumption that overaging metastable precipitates are not existent, as the measurements did not show them in an amount capable of altering the result. If the were to be present, the expectation is that the volume fraction if β'' precipitates would be lower to accommodate them in the total balance.

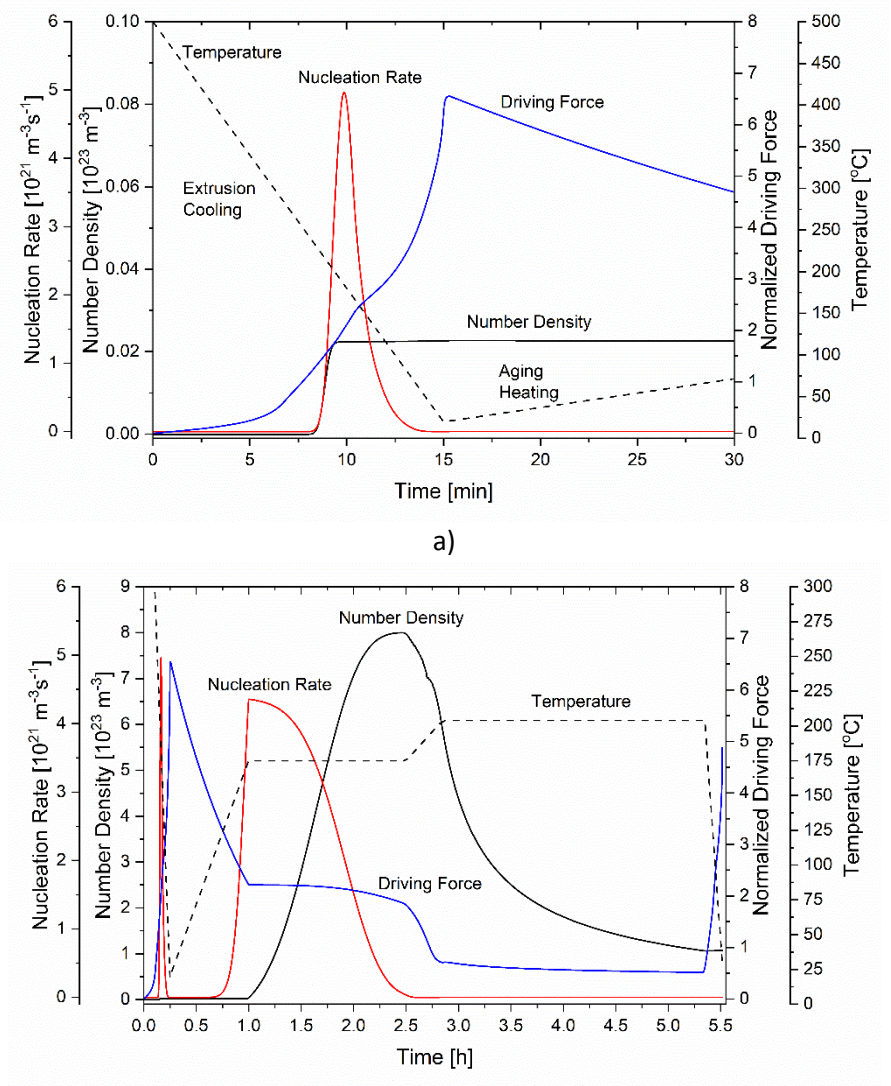

Figure 17: Evolution of Number Density, Nucleation Rate and Normalized Driving Force for precipitation during a) extrusion cooling and b) aging.

4.2 Aging Simulation Results

After extrusion cooling the material is subjected to aging in order to form a very fine dispersion of β'' particles that provide strength to the extruded profile. As explained in section 1.2, natural aging in the time that the material is stored at room temperature. For

this case, natural aging occurred between extrusion cooling and aging but measurements showed no effect to the final microstructure, so it was omitted from the calculations. As the temperature rises, initially the microstructure remains relatively unchanged, as the nucleation rate remains close to zero and the number density of β'' needles maintains a constant low value. This is due to sluggish diffusion at low temperatures, inhibiting the nucleation of new and the growth of preexisting particles, even though the chemical driving force for precipitation is relatively high, as shown in Figure 17 b). Similarly, the volume fraction remains close to zero and the mean needle length and radius maintain a constant value as presented in Figures 18 and 19.

Right before the material reaches the first holding temperature, the nucleation rate rises almost instantly to its max value and then smoothly decreases. Although the driving force decreases ever so slightly the number density of β'' precipitates keep increasing, as it still is high enough for nucleation and growth to continue. This is clearly portrayed in Figure 17 b). Although new precipitates are created, their critical radius is very small, thus they have a late effect on the volume fraction, as shown in Figure 18 and 19. The size distribution of needle radii and lengths, by the end of the first heating stage is shown in Figure 21 a) and b) respectively. Compared to the distribution at the end of extrusion cooling, the distribution at the end of heating is more spread out resulting in a lower peak value yet a larger total number density of particles.

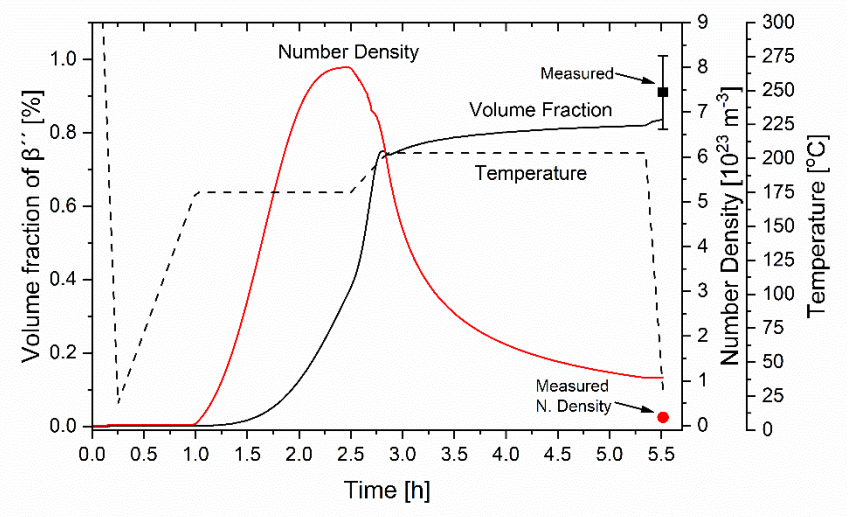

Figure 18: Evolution of the Volume Fraction and Number Density of β'' needles.

During the 2nd isothermal holding, the nucleation of new particles and growth of preexisting ones, is promoted. As presented in Figure 17 b), during the second nucleation event, the nucleation rate of β'' needles is elevated at first, gradually decreasing and approaching zero as the precipitation progresses. Consequently, the number density of particles continuously increases, reaching a maximum value by the end of the isothermal holding. The driving force for precipitation remains relatively constant at first, gradually decreasing at the end of the isothermal section, as the temperature remains constant and the supersaturation of Mg and Si in the matrix diminishes due to the formation of β'' needles, as shown in Figure 20. As a result of the increased nucleation rate, the volume fraction of β'' needles continuously increase, as presented in Figure 19. The critical radius of the nuclei that form is very small and as a result the mean radius and needle length rapidly decreases at first stages of the

isothermal treatment, as shown in Figure 20. However, the mean radius and needle length gradually increase throughout isothermal holding, as a result of particle growth. This is also evident in the size distributions of Figure 21, where by the end of the isothermal section, a bimodal distribution has formed. The first small spike located at approximately r = 0.4nm, corresponds to the size of the critical radius r_c of the nucleating particles, whereas the second broad peak of the distribution at r = 1nm, corresponds to the particles that nucleated and grew over the course of the isothermal holding. There is also a very small peak, located at r = 1.8nm, which corresponds to particles that precipitated during extrusion cooling and grew during heating and isothermal holding. Since the number density of those particles is very small, the peak is barely visible in the graph, thought it becomes more pronounced at later stages of processing.

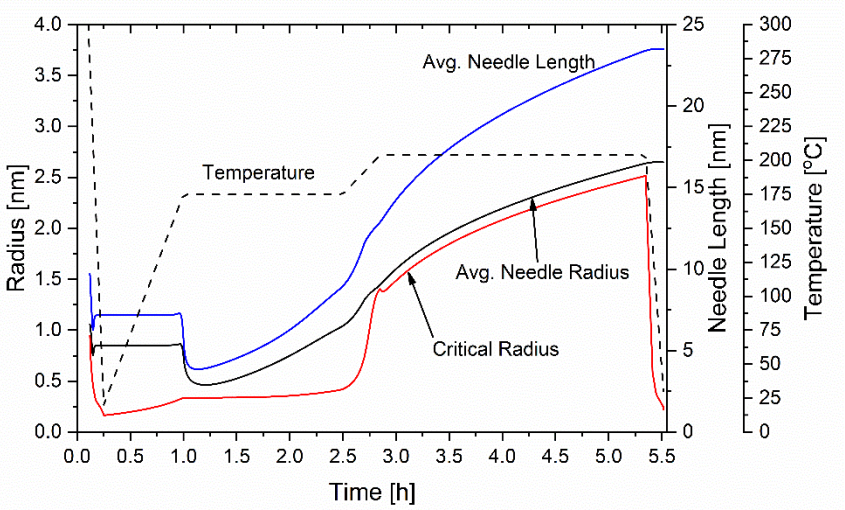

Figure 19: Evolution of the average radius and length of β'' needles, along with the critical radius for particle nucleation.

During the second isothermal holding period, the nucleation rate remains almost zero, indicating that new particles are not nucleated, as shown in Figure 17 b). The driving force for precipitation decreases with the increase in temperature during heating and then stays relatively constant with a very gradual downwards draft as the Mg and Si concentration in the matrix decreases due to needle growth, as it can be observed in Figure 20. The driving force for precipitation remains positive, promoting the growth of β'' needles and as a result the volume fraction rapidly increases, especially during the heating stage, shown in Figure 18. However, the number density continuously decreases, under the influence of the minimization of the surface and strain energy of β'' needles, promoting the dissolution of smaller particles and the growth of larger ones. As a result, many small nuclei that formed during the first isothermal treatment, are dissolved back in the matrix, whereas the larger ones grow even larger. This mechanism is favorable to reaching peak hardness in the final product. The effect is also evident in Figure 19 and 21, where by the end of heating the size distribution has moved to the right due to particle growth and particles at the left side of the distribution have vanished, resulting in an increase of the mean radius and needle length. During the second isothermal holding the volume fraction of β'' gradually increases, whereas the number density continuously decreases as small particles dissolve.

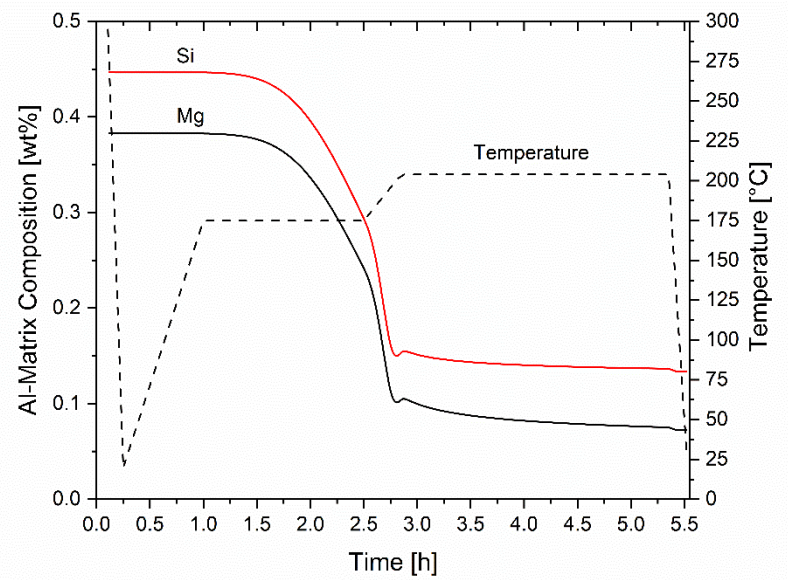

Figure 20: Evolution of the Mg and Si concentration in the aluminum matrix throughout extrusion cooling and aging.

Finally, at the end of the second isothermal holding, rapid cooling to room temperature takes place. Since the cooling rate is large, the material is cooled quickly and no significant microstructural changes occur. The volume fraction slightly increases due to growth, without the nucleation of new particles as the nucleation rate remains almost zero. After cooling the total volume fraction of β'' particles very close to the measured value of TEM measurements. Even though the Mg and Si concentration is reduced in the aged condition compared to as cast condition, the remaining concentration in the matrix is high enough to suggest that the β'' fraction could be increased, for a closer match with the experimental values. The distribution of the radius and length of β'' needles after cooling from aging is presented in Figure 21. During the second isothermal holding, a bimodal distribution of particles forms, that is maintained upon cooling. As needle growth occurs at elevated temperatures, the radius and length increases, forming a broad skewed distribution towards large particles. The second peak of the distribution, in Figures 21 a) and b) respectively, correspond to particles that nucleated during extrusion cooling and grew upon aging. In practice, this peak would be comprised of the overaging precipitates (β', U1, U2 and B') on dispersoids and grain boundaries, if they were considered in the extrusion cooling calculations.

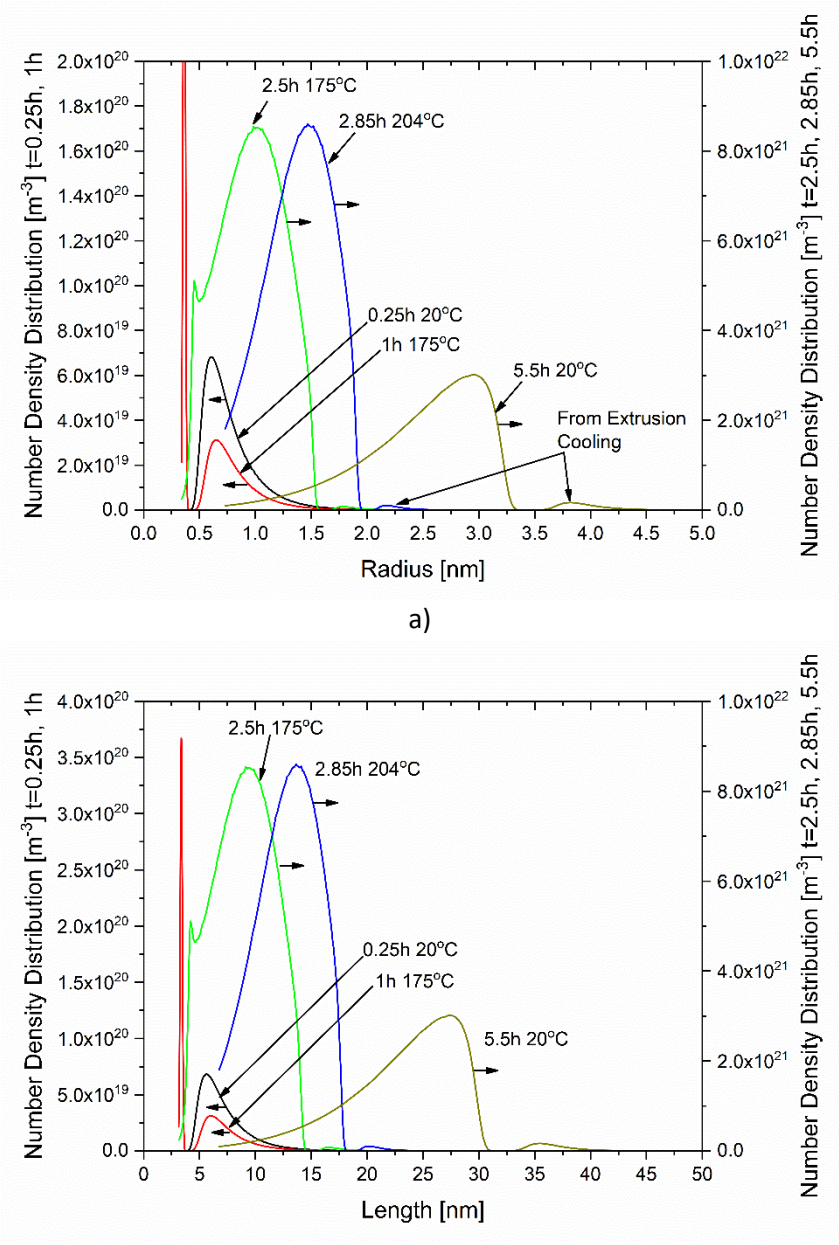

Figure 21: Distribution of needle a) Radii and b) Lengths at different time intervals throughout processing. The left axis corresponds to extrusion cooling and aging heating at t=0.25 and 1h, whereas the right axis to aging at t=2.5, 2.85 and 5.5h

4.3 Yield Strength Simulation Results

Total yield strength of the material is comprised of individual stresses, mainly grain boundary, forest dislocation, solid solution and precipitation hardening. All the above are shown in Figure 22 as a function of time during extrusion cooling and aging. As seen in Figure 22, grain boundary and forest dislocation stress remain constant throughout the whole process, as the matrix grain diameter and dislocation density are not affected by extrusion cooling and aging. Solid solution strengthening is related to the matrix supersaturation of Mg and Si. As shown in Figure 21 and 22 , it decreases according to the

decrease in Mg and Si concentration of the matrix. During extrusion cooling the minimal precipitation of β'' needles, causes a slight increase in yield strength through precipitation strengthening that coincides exactly with the measured value. Afterwards, the total yield strength enters a plateau up until the first holding temperature is achieved and diffusion commences again. At that moment, precipitation of very fine β'' needles begins and the supersaturation of Mg and Si in the matrix decreases, and so change their effects on total yield strength. From there and until the end of aging, the total yield strength increase is entirely attributed to precipitation strengthening and so it follows the exact same rate, as presented in Figure 22 The final value totally reflects the measured one. According to the literature [2,18,19] the critical radius where the precipitation strengthening mechanism transitions from coherency to Orowan hardening, ranges from 1.8 to 5nm depending on the strengthening precipitate and alloy composition. In the present study a value of $2.8nm$ was adopted. The average radius of the needles at the end of aging is $2.65nm$, indicating that the majority of particles remain shearable by dislocations and the primary precipitation strengthening mechanism is coherency hardening. This leads to the conclusion that the material is very close to peak attainable hardness and the aging procedure is well planned.

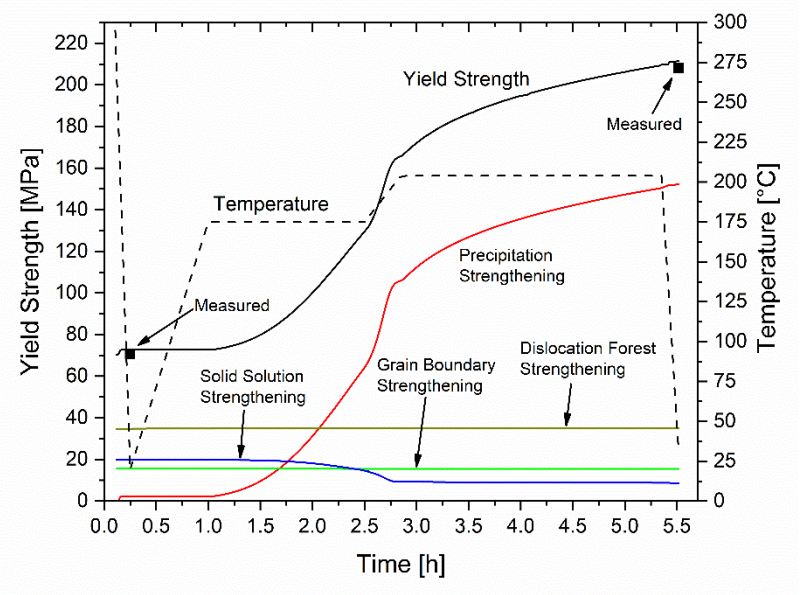

Figure 22: Evolution of the yield strength as a function of time during processing.

4.4 Precipitation Model Validation

In order to verify the validity of the KWN precipitation calculations and simulation results for the precipitation and yield strength models, a comparison between experimental data is necessary. Characterization of the as extruded and aged material was performed by SINTEF using SEM/EDX and TEM analysis, as discussed in detail in section 3. The mechanical behavior of the as extruded and aged material was performed in the Laboratory of Mechanics and Strength of Materials at the University of Thessaly and is presented in detail in section 4. A summary of the comparison between simulated and predicted results is given in Table 5. In general, there is very good agreement of the model predictions with the

available experimental data. For the extruded material, the only comparable value is the yield strength, which value is very close to the experimental one. For the aged material, due to the TEM characterization , more data are available for comparison. As provided by Table 5, volume fraction, number density and mean particle radius values of β'' needles are very close between calculated and experimental. The KWN model though presents a limitation in the needle length calculation process, as it is corelated to the particle radius value through a constant aspect ratio. This essentially bonds the needle length to the needle radius. It also has an effect on the number density as for the same volume fraction, if the needle length was bigger, the number density would be lower. This is the reason for the discrepancies observed in needle length and number density in Table 5.

Table 5: Comparison between experimental and simulation results regarding the as extruded and aged materials.

	Measured	Predicted
	As Extruded Material	
$Yield\ Strength\ (MPa)$	70.5	72.8
	Aged Material	
$Volume\ fraction\ of\ \beta''\ f_{\beta''}(^0/_0)$	0.91	0.837
$Number\ Density\ of\ \beta''\ \ N(m^{-3})$	1.85 10^{22}	1.08 10^{23}
$Mean\ Radius\ \bar{r_d}\ (nm)$	2.83	2.65
$Mean\ Length\ \bar{L}(nm)$	40	23.5
$Yield\ Strength\ (MPa)$	208	211

The probability density function (PDF) of the needle cross-sectional area and length distributions, at the end of aging, according to quantitative TEM observations and KWN simulation results, are presented in Figure 24. In accordance with the values in Table 5 , the cross sectional area distribution of β'' particles is in perfect alignment with the values measured by TEM. This is bound to the rhomboidal cross section of β'' particles and that the calculated radius corresponds to the large diameter of the rhombus. On the contrary, the needle length is not portrayed correctly, for the reasons mentioned above. The calculated values are into a less broad distribution and to lower length needles than the measured from TEM. The biggest divergence occurs as the particles grow and the needle length gets bigger. This results in an underestimation of the needle length and an overestimation of the number density in the final results. Nevertheless, the most important factors for the final mechanical properties are the volume fraction of β'' needles and the radius distribution, so the needle length and number density discrepancy is not taken into account.

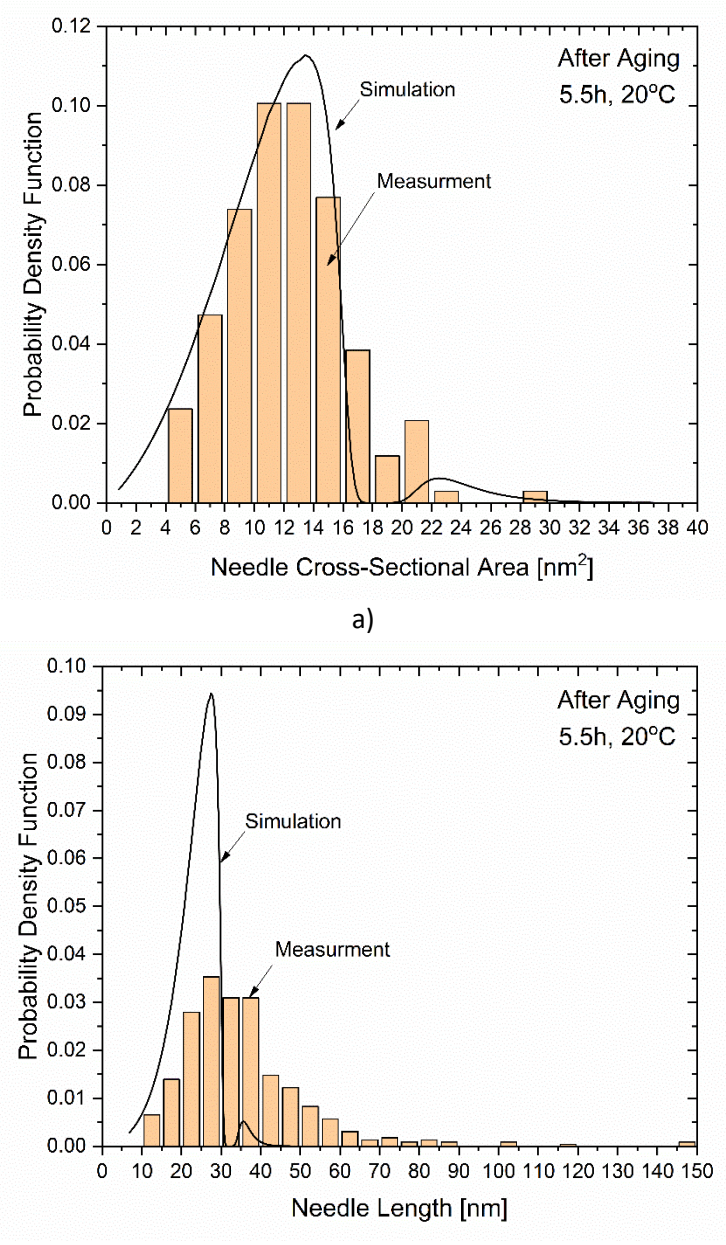

Figure 23: Comparison of the simulated and measured probability density functions of the a) needle cross-sectional area and b) length distributions, after aging.

4.5 Flow stress model validation

As mentioned in section 2.2.2, the predictive model for the flow stress created, should be confirmed is its accuracy. This can be done natively through the model itself, as experimental data are supplied to it for its initial calibration. An indication of proper calibration and calculations is the workhardening of the material. As it is shown in Figures 24 and 25, the workhardening phase of the aged material, portrayed with yellow arrows is exactly on the path of the stress-strain curves produced by the experimental data. Moreover, the optimization plot shoes that the optimal values were reached within a very limited number of iterations for both calculating methods (Mean Squad and Mean Absolute

Errors). This means that provided accurate measurements of volume fraction and particle radius, the model can accurately predict the flow stress development of any aluminum alloy, in any condition from as cast material to aged condition.

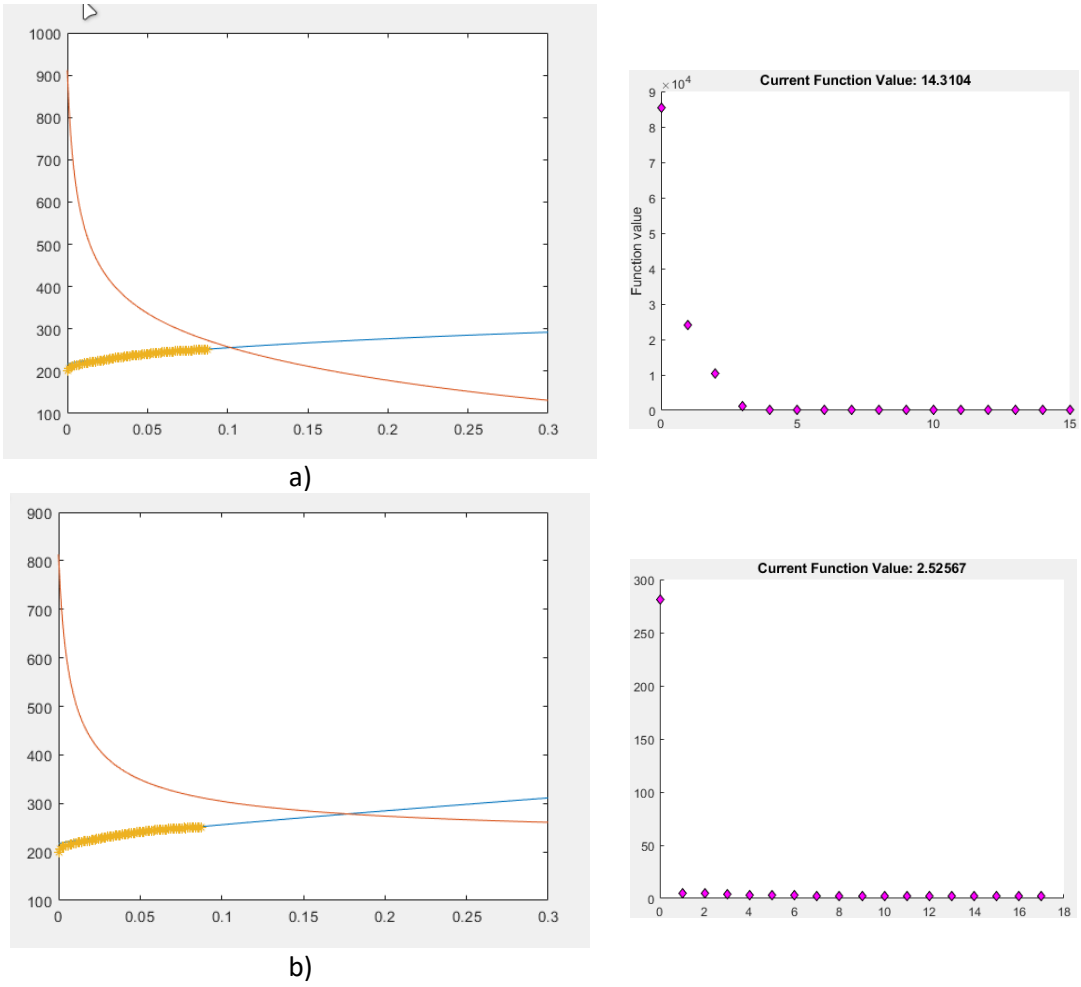

Figure 24: Flow stress model results and optimization plots for aged smooth specimen 1 calculated with a) Mean Squared Error and b) Mean Absolute error

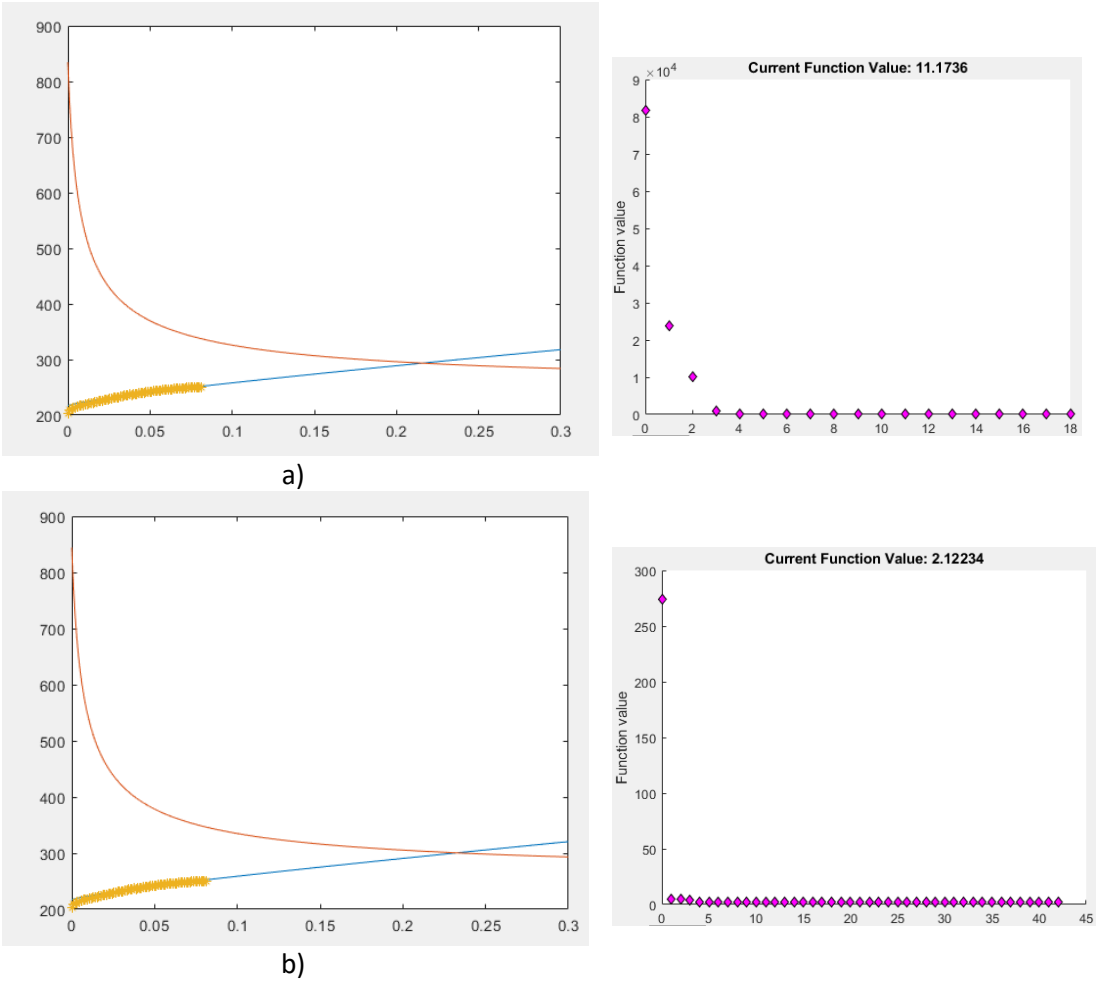

a)

b)

Figure 25: Flow stress model results and optimization plots for aged smooth specimen 2 calculated with a) Mean Squad Error and b) Mean Absolute error

5. Conclusions

During this study, the general behavior and the characteristics of 6xxx aluminum alloys were explored, especially of the 6060 alloy. The main focus of the study was the microstructural changes after extrusion and during aging of the materials. Experimental specimens were analyzed by TEM and SEM/EDX methods by SINTEF in order to provide a clear view on their microstructure and a comparison between material provided by Alumil and material produced by the Laboratory of Mechanics and Strength of Materials at the University of Thessaly took place.

For the extruded specimens, the SEM- EDX analysis by SINTEF revealed that there were not any β-Mg_2Si particles on large dispersoids or in grain boundaries. However, there was a strong presence of metastable overaging β-family precipitates such as β', U1, U2 and B' on dispersoids and grain boundaries, as TEM analysis of the aged material revealed. These particles, precipitated during extrusion cooling and are linked with the creation of PFZs. Extensive and rather large PFZs were observed in the final, aged material. PFZs are zones in

the material where the wanted fine dispersion of β'' needles is not achieved, usually around dispersoids and grain boundaries. This reduces the overall ductility of the material and may lead to premature failures. The solution to mitigate the creation of PFZs, is the accelerated cooling rate after extrusion, in order to avoid the migration of Mg and Si atoms through the matrix, and possibly improve the final mechanical properties.

In the aged conditions, TEM measurements showed that a very fine dispersion of β'' needles was achieved. The particles were found to be small and fully coherent with the matrix, impeding dislocation movement and providing strength to the material. The simulations via computational thermodynamic and precipitation kinetics calculations conducted by the Laboratory of Mechanics and Strength of Materials at the University of Thessaly gave a more detailed perspective on the precipitation procedure. The particles that precipitate during extrusion cooling are minimal, as the cooling rate is fast enough to hamper diffusion. The aging procedure is identified as double T5, meaning that the material undergoes 2 consecutive isothermal holdings. Diffusion continues during the first heating of aging, and the existing percipitates enlarge. During the first isothermal holding more particles precipitate but the coarsening is not very prominent , and the effects on the total material strength are minimal. During the second holding though, the volume fraction of the β'' needles is found to rapidly increase, as the existing particles grow. This results in an increase to the needle length and radius. Simultaneously the smaller particles that did not grow, dissolve in the matrix and number density (number of particles per unit volume) decreases. As the particle radius grow, the effect on the yield strength is increasing due to coherency hardening. The peak strength of the material is achieved on the brim of overaging, right before the Orowan mechanism activates and coherency loss occurs. TEM and precipitation calculations confirmed that on this case, the material is slightly underaged, thus very close to peak attainable hardness. Tensile test carried by the Laboratory of Mechanics and Strength of Materials at the University of Thessaly confirmed that simulations were in perfect agreement with the TEM data by SINTEF.

Finally, tensile tests with notched and smooth specimens were conducted for extruded and aged materials by the Laboratory of Mechanics and Strength of Materials at the University of Thessaly. The stress-strain response was measured, along with the yield strength, UTS, uniform elongation, total elongation and workhardening rate. Notched specimens were utilized in order to study the mechanical behavior under high stress triaxiality conditions, important when ductility under high strain rates, toughness and crash resistance is of interest. These data were then utilized for the creation and calibration of the flow stress model presented in the study.

6. Bibliography

1. Nedal-alloy-Datasheet-EN-AW-6060.
2. Sarafoglou, P. I., Serafeim, A., Fanikos, I. A., Aristeidakis, J. S. & Haidemenopoulos, G. N. materials Modeling of Microsegregation and Homogenization of 6xxx Al-Alloys Including Precipitation and Strengthening During Homogenization Cooling. doi:10.3390/ma12091421.
3. Study of the effect of aging condition on strength & hardness of 6063…. https://www.slideshare.net/anushkauom/study-of-the-effect-of-aging-condition-on-strength-hardness-of-6063-t5-alloy.
4. Γρηγόρης Ν. Χαϊδεμενόπουλος. *Φυσική Μεταλλουργία*. (Εκδόσεις Τζιόλα, 2007).
5. Thermo-Calc AB. Precipitation Module (TC-PRISMA) User Guide. (2021).
6. Wagner, R., Kampmann, R. & Voorhees, P. W. Homogeneous Second-Phase Precipitation. *Phase Transformations in Materials* 309–407 (2005) doi:10.1002/352760264X.CH5.
7. Langer, J. S. & Schw3, J. PHYSICAL REVIE% A VO LUME 21, NUMBER 3 M ARC H 1980 Kinetics of nucleation in near-critical Anions.
8. Russell, K. C. Nucleation in solids: The induction and steady state effects. *Advances in Colloid and Interface Science* **13**, 205–318 (1980).
9. Lee, S., Estrin, Y. & de Cooman, B. C. Constitutive modeling of the mechanical properties of V-added medium manganese TRIP steel. *Metallurgical and Materials Transactions A: Physical Metallurgy and Materials Science* **44**, 3136–3146 (2013).
10. Zander, J., Sandström, R. & Vitos, L. Modelling mechanical properties for non-hardenable aluminium alloys. *Computational Materials Science* **41**, 86–95 (2007).
11. Andersen, S. J., Marioara, C. D., Friis, J., Wenner, S. & Holmestad, R. Precipitates in aluminium alloys. (2018) doi:10.1080/23746149.2018.1479984.
12. Holmestad, R. *et al.* Precipitation in 6xxx Aluminum Alloys.
13. Ninive, P. H. *et al.* Detailed atomistic insight into the β″ phase in Al-Mg-Si alloys. *Acta Materialia* **69**, 126–134 (2014).
14. Chen, H. *et al.* Atomic scale investigation of the crystal structure and interfaces of the B′ precipitate in Al-Mg-Si alloys. *Acta Materialia* **185**, 193–203 (2020).
15. Milkereit, B. & Starink, M. J. Quench sensitivity of Al-Mg-Si alloys: A model for linear cooling and strengthening. *Materials and Design* **76**, 117–129 (2015).
16. Strobel, K., Easton, M. A., Sweet, L., Couper, M. J. & Nie, J.-F. Relating Quench Sensitivity to Microstructure in 6000 Series Aluminium Alloys * 1. doi:10.2320/matertrans.L-MZ201111.

17. Myhr, O. R., Grong, Ø., Fjaer, H. G. & Marioara, C. D. Modelling of the microstructure and strength evolution in Al-Mg-Si alloys during multistage thermal processing. (2004) doi:10.1016/j.actamat.2004.07.002.

18. Bardel, D. *et al.* Coupled precipitation and yield strength modelling for non-isothermal treatments of a 6061 aluminium alloy. *Acta Materialia* **62**, 129–140 (2014).

19. Zander, J. & Sandström, R. One parameter model for strength properties of hardenable aluminium alloys. *Materials and Design* **29**, 1540–1548 (2008).